Measurement Report: New particle formation characteristics at an urban and a mountain station in Northern China

Ying Zhou[1], Simo Hakala[2], Chao Yan[1,2,*], Yang Gao[3], Xiaohong Yao[3], Biwu Chu[4], Tommy Chan[2], Juha Kangasluoma[1,2], Shahzad Gani[2], Jenni Kontkanen[2], Pauli Paasonen[2], Yongchun Liu[1], Tuukka Petäjä[2,5], Markku Kulmala[1,2], Lubna Dada[2,6,7*]

[1] Aerosol and Haze Laboratory, Beijing Advanced Innovation Center for Soft Matter Science and Engineering, Beijing University of Chemical Technology, Beijing, China

[2] Institute for Atmospheric and Earth System Research / Physics, Faculty of Science, University of Helsinki, Finland

[3] Key Laboratory of Marine Environment and Ecology, Ministry of Education, Ocean University of China, Qingdao 266100, China

[4] State Key Joint Laboratory of Environment Simulation and Pollution Control, Research Center for Eco-Environmental Sciences, Chinese Academy of Sciences, Beijing 100085, China

[5]Joint International Research Laboratory of Atmospheric and Earth System Sciences (JirLATEST), Nanjing University, Nanjing, China

[6]Extreme Environments Research Laboratory, Ecole Polytechnique Fédérale de Lausanne (EPFL) Valais Wallis, Sion, 1951, Switzerland

[7]Laboratory of Atmospheric Chemistry, Paul Scherrer Institute, 5232 Villigen, Switzerland

Correspondence to: Lubna Dada: lubna.dada@helsinki.fi & Chao Yan: chao.yan@helsinki.fi

Abstract

Atmospheric new particle formation (NPF) events have attracted increasing attention for their contribution to the global aerosol number budget, and therefore their effects on climate, air quality, and human health. NPF events are regarded as a regional phenomenon, occurring over a large area. Most observations on NPF events in Beijing and its vicinity were conducted in populated areas, whereas observations on NPF events on mountaintops with low anthropogenic emissions are still rare in China. The spatial variation of NPF event

intensity has not been investigated in detail by incorporating both urban areas and mountain measurements in Beijing. Here, we provide NPF events characteristics in summers 2018 and 2019 at urban Beijing and a comparison of NPF event characteristics — NPF event frequency, formation rate, and growth rate — by comparing an urban Beijing site and a background mountain site separated by ~80 km from June 14 to July 14, 2019 as well as giving insights into the connection between both locations. There were no significant difference of formation rates and growth rates observed during the short-term observation in 2019 and longer-term observation in summers 2018 and 2019 at the urban site. During parallel measurements at urban Beijing and mountain background areas, although the median condensation sink during the first two hours of the common NPF events was around 0.01 s^{-1} at both sites, there were notable differences in formation rates between the two locations (median of 5.42 $cm^{-3}s^{-1}$ at the urban site and 1.13 $cm^{-3}s^{-1}$ at the mountain site during the first two hours of common NPF events). In addition, the growth rates in the 7-15 nm range for common NPF events at urban site (median of 7.6 $nm.h^{-1}$) were slightly higher than those at mountain site (median of 6.5 $nm.h^{-1}$). To understand whether the observed events were connected, we compared air mass trajectories as well as meteorological conditions at both stations. Favorable conditions for the occurrence of regional NPF events were largely affected by air mass transport. Overall, our results demonstrate a clear inhomogeneity of regional NPF within a distance of ~100 km possibly due to the discretely distributed emission sources.

Keywords: atmospheric aerosols, growth rates, regional new particle formation, sulfuric acid

1 Introduction

Atmospheric new particle formation (NPF) events resulting from the formation of clusters and stable aerosol particles from gas-phase precursors have been recognized as a major contributor to the global aerosol budget (Kulmala et al., 2004; Zhang et al., 2012). Once the newly formed particles grow to certain sizes, they can act as cloud condensation nuclei (CCN), affecting the regional and global climate (Pierce and Adams., 2009;Yu and Luo., 2009). NPF events were also found to contribute to haze formation and thus can influence air quality, especially in megacities where the precursor concentrations and associated formation rates are rather high (Guo et al., 2014; 2020;Kulmala et al., 2021;Du &Dada et al., 2021).

The occurrence of NPF events is a result of the competition between factors promoting and inhibiting cluster formation and their growth. For instance, sufficient sulfuric acid and other low-volatility vapors have been

confirmed to be important in particle nucleation and growth in field observations as well as in chamber experiments (Ehn et al., 2014;Wang et al., 2017;Lehtipalo et al., 2018;Yao et al., 2018;Deng et al., 2020b). On the other hand, background particles can inhibit new particle formation by acting as condensation sink for vapor precursors and coagulation sink for newly formed particles. Indeed, Cai et al. (2017) found that the Fuchs Surface Area (A_{Fuchs}) (which is linearly proportional to condensation sink) determined the occurrence of NPF events in urban Beijing. In the atmosphere, ambient conditions, such as air mass trajectories and meteorological conditions, can affect the occurrence of NPF events by modifying the source-sink competition. Wu et al. (2007) summarized favorable conditions for NPF events in Beijing based on a one-year observation as sufficient solar radiation (sunny days), northerly wind, low relative humidity, and less pre-loading large particles. Similarly, in other environments, plenty of radiation, intermediate temperatures and low condensation sink favor the occurrence of NPF events (Qi et al., 2015; Dada et al., 2017; Kerminen et al., 2018). Regional NPF events can happen with a spatial extent up to several hundred kilometers and vertical extent from boundary layer to free troposphere under favorable conditions (Hussein et al., 2009; Shen et al., 2011; Dai et al., 2017). Earlier studies have shown that regional NPF events by simultaneous observations at two or more sites had similar features in their occurrence and characteristics. For instance, Komppula et al. (2006) investigated the occurrence of NPF events at two forest stations in northern Finland during 2000-2003. Their results suggested that same air mass source regions, favorable weather conditions and clean air at both stations were necessary for NPF events occurring simultaneously at the two stations. Vana et al. (2016) compared observations at three sites over 1000 km distance at northern Finland, southern Finland and Estonia in 2013-2014. They found that some events have the same origin. On the other hand, Jun et al. (2014) observed that NPF events occurred less frequently at downtown Toronto than at a nearby background site, and attributed this observation to the high condensation and coagulation sink due to primary particle emission from traffic at urban areas. Moreover, Carnerero et al. (2018) observed horizontal distribution and regional impact of the NPF events with data from three urban, urban background, and suburban stations in the Madrid metropolitan area, Spain in July 2016. Their results indicated that ultra-fine particles were detected quasi-homogenously in an area spanning at least 17 km horizontally and the NPF events extended over the full vertical extension of the mixed layer. Finally, Salma et al. (2016) found that regional NPF events were modified and transformed by urban NPF events during their observation in 2008-2009 and 2012-2013 in Budapest and at a regional background site 71 km away from it. In comparison to

the aforementioned studies in Europe, a similar study was also carried out to understand the regional NPF events in North China Plain. Wang et al. (2013) characterized the NPF events observed at an urban Beijing site and a regional background site about 120 km northeast to the urban site from March to November in 2008. They observed 96 and 87 NPF events at urban Beijing and background site, respectively, among which 52 NPF events were observed simultaneously at both sites. They found that NPF events were slightly weaker in the background site compared to those observed at the urban site. However, the factors that influence the occurrence of NPF events at the two stations simultaneously were left undetermined.

In addition to horizontal extension of NPF events, the vertical extension of NPF events also attract attention of researches. It have been confirmed that NPF events can be triggered within the whole low tropospheric column at the same time and even above the planetary boundary layer upper limit (Boulon et al., 2011). Sellegri et al. (2019) reviewed NPF events observed at 6 different altitude stations. They found NPF events was most favored at the altitude close to the interface of the free troposphere (FT) with the planetary boundary layer (PBL) and at the vicinity with clouds. In addition, at high altitude sites, CS may not be the liming factor for NPF occurrence as higher CS associated with more precursors for nucleation and initial growth. Based on observations at two different altitudes (e.g. 340 m and 560 m above sea level) in northern Finland, Komppula et al. (2003) found NPF events had similar formation and growth rates between these two heights, while due to vertical movement of air masses, difference of NPF event start time between these two sites was limited within 30 min. Similar results were also observed at two sites in France that formation and growth rates were similar between two altitudes (e.g., 660 m and 1465 m above sea level) while the contribution of ion-induced nucleation was higher at high altitude (Boulon et al., 2011). Finally, during a recent observation in Spain, growth rates were higher at the mountain site (2500 m a.s.l.) than urban site (680 m a.s.l.), while difference between formation rates varied with altitude.

In addition to largely populated urban areas, there is a large mountain area within the Beijing-Tianjin-Hebei (BTH) region, where to our best knowledge, the characteristics of NPF events are understudied. In this study, we conducted simultaneous measurements of NPF event characteristics at an urban site in Beijing and a background mountain site about 80 km west to urban Beijing from June 14 to July 14 2019.

Based on our observations, we aim to (i) compare the characteristics of the NPF events between the two sites, including the frequency, formation rate, and growth rate; (ii) figure out the connections and differences between

NPF events at these two sites; (iii) identify the favorable conditions for regional NPF events. Due to the profound participation of NPF events in the global aerosol number loading and air quality degradation, identifying the conditions those promote or inhibit the occurrence of regional scale NPF events could help to minimize its adverse effects.

2 Experiment and methodology

2.1 Measurement sites' description

Urban site: The Beijing University of Chemical Technology - BUCT (39.94° N, 116.31° E) station is located on the fifth floor of a university building inside the west campus of BUCT. The station is surrounded by several main roads with heavy traffic and residential areas and thus, can be considered a typical urban station. The altitude of the west campus of BUCT is around 20 m above sea level and the urban site is around 12 m above ground level. More details of this station can be found in Zhou et al. (2020). Observations at the urban site are continuous since January 17, 2018 and were only interrupted for necessary instrument maintenance. The location is referred to as '**UB**' from here after and is shown on the map in Figure 1.

Mountain site: The Beijing Forest Ecosystem Research Station (39.96° N, 115.43° E) is located in the west of Beijing, referred to as '**MT**' from here after, which is part of the Chinese Ecological Research Network (CERN). It is located in the mountain areas west of Beijing, about 80 km from the urban site; see also in Figure 1. The altitude of the station is 1170 m above sea level and it is surrounded by forests. The closest anthropogenic activities are associated with small villages located in the valley nearby the MT station. Observations at MT station are from June 14 to July 14, 2019. For comparison reasons, we only used the data collected simultaneously at both stations.

Longquan station: The Longquan national monitoring station sits in Longquan town, Mengtougou District, Beijing. It is 20 km west to UB site and 60 km east to MT site and considered as a suburban station. The location is referred to as '**LQ**' from here after and is shown on the map in Figure. 1.

2.2 Instrumentation

As shown in Figure 2, the data qualities of particle number size distribution at both sites during the short-term parallel observations was good in general. Particle number size distribution data in the size range of 6-840 nm

were collected using a differential mobility particle sizer (DMPS) at the UB station. The instrument consists of one Hauke-type DMA (differential mobility analyzer, home-built by university of Helsinki) in different flow rates and one CPC (condensation particle counter, TSI Model 3772). Details of this instrument can be found in Salma et al. (2011) and Kangasluoma et al. (2020). At MT station, a scanning mobility particle sizer (SMPS, consists of a TSI Differential Mobility Analyzer model 3081) and a fast mobility particle sizer (FMPS, TSI Model 3091) were used to measure particle number size distribution from June 14 to June 28 and from June 29 to July 14, respectively. The size ranges of the SMPS and FMPS are 7-1218 nm and 6.04-856 nm, respectively. The total number concentration from 4-3000 nm, measured by Condensation Particle Counter (CPC; TSI Model 3775), was used to calibrate the particle number size distributions from FMPS according to the method suggested by Zimmerman et al. (2015). More details about the instrument are found in the previous studies (Wang et al., 2019; Gao et al., 2020). The particle number size distribution measured by FMPS correlated well with SMPS during the comparison in laboratory after being calibrated (Lee et al., 2013).

To ensure high quality of particle number size distribution data at UB site, a particle number size distribution system (PSD) also sampled in parallel with DMPS from June 1 to August 31, 2019 (summer 2019). It included a nano-scanning mobility particle sizer (nano-SMPS, 3–55 nm, mobility diameter), a long SMPS (25–650 nm, mobility diameter) and an aerodynamic particle sizer (APS, 0.55–10 μm, aerodynamic diameter). Details of this instrument can be seen at Liu et al. (2016) and Deng et al. (2020b).

The PSD was used as a reference. As shown in Figure 3, median particle number size distribution obtained from PSD and DMPS matched well in data trend. Varying with particle diameter, particle number size distribution data measured by DMPS can be higher or lower than PSD within a factor of 2.

We cannot compare particle number size distribution data obtained from DMPS, SMPS and FMPS as we did not sample with these three instruments in parallel at the same site. However, it is reasonable to assume that particle number size distribution obtained from FMPS were comparable with those from DMPS as on one hand the measurement techniques of particle number size distribution in the size range of these two instruments have been well developed and be applied in quite a lot observations (Wang et al., 2017; Kangasluoma et al., 2020), on the other hand, the particle number size distribution from FMPS was carefully calibrated and the FMPS was properly operated during the observation as discussed above. Similar conclusions apply for the SMPS as well where we can rely on using the measurement from this instrument to discuss at least NPF event frequency at MT

site during June 14 to June 28, 2019, during which parameters of only one NPF event are calculated.

Sulfur dioxide (SO_2) concentration data were collected by Thermo Environmental Instrument model 43i-TLE with a time resolution of 5-min at the UB station. There were no direct measurement of SO_2 concentrations at the MT station, but the SO_2 measurement at the closest national monitoring station (Longquan station, around 60 km from MT station and 20 km from UB station, see Figure 1) was used to indicate the strong decline of SO_2 concentration from urban Beijing towards the west areas. Time series of SO_2 concentration at UB station and Longquan station during the whole observation is shown in Figure 4. Due to the lower emission, the SO_2 concentration at the MT station is expected to be even lower than that in Longquan station.

The sulfuric acid concentration was measured at UB station by a chemical ionization-atmospheric interface-time of flight mass spectrometers (CI-APi-ToF, Aerodyne Research Inc.) equipped with a nitrate chemical ionization at UB station (Lu et al., 2019). There were no sulfuric acid data available at MT station and since no SO_2 concentrations were available, a sulfuric acid proxy concentration could not be derived.

The meteorological conditions such as relative humidity (RH, %), temperature (°C) and solar radiation (UVA and UVB, W/m^2) were measured using a Vaisala Weather station data acquisition system (AWS310, PWD22, CL51), Metcon at UB station and using Vaisala MAWS301 automatic weather station at MT station. The measurements at the MT station were carried out at the height of 1.5 m. The wind speed (m/s) and wind direction (°) data were also measured by the weather station at UB site, while at MT site, we obtained with reanalyzed data from ERA5 model (Olauson, 2018).

2.3 Air mass back trajectories

Air mass back trajectories were calculated using a Lagrangian particle dispersion model FLEXPART (FLEXible PARTicle dispersion model) version 9.02 (Stohl et al., 2005). As the meteorological input, we used ECMWF (European Centre for Medium-Range Weather Forecast) operational forecast data with 0.15° horizontal and 1-hour temporal resolution. Particle retroplume simulations were performed hourly for both sites during the whole study period. For each retroplume simulation, we used 50 000 model particles distributed evenly between 0–100 m above the measurement site. The released model particles were traced backwards in time for 72 h, unless they exceeded the model grid (20–60°N, 95–135°E, resolution: 0.05°).

Based on the arrival direction of the 72-h backward trajectories, the prevailing air mass transport conditions at

each site were classified into 5 groups: North group, West group, East group, South group and Local group. Air masses arriving from north, north-west and north-east including Mongolia, Inner-Mongolia and north-east China were classified into the North group. Air masses from Shanxi province, Inner-Mongolia and further west were classified into the West group. Air masses from the ocean east of Beijing were classified into the East group and air masses from southern areas were classified into the South group. Stagnant air masses that had only travelled short distances and/or were circulating around the measurement site were classified into the Local group. Examples of air mass trajectories belonging to these five groups are shown in Figure 5. In general, air masses from the north and west supply clean air from the mountainous areas to both stations, whereas air masses from the east and south travel over highly populated areas, thus accumulating air pollutants. However, the impact of local air masses on the pollution levels at the two sites can be different; at UB station, local air masses are polluted by the urban emissions, while at MT station stagnant air could cause a clean situation due to low local emissions. More details on the relationship between air mass transport conditions and the extent of pollution is discussed in later sections.

2.4 Estimating the spatial extent of NPF

The observation of regional new particle formation events, where the growth of newly formed particles can be followed for several hours, is a result of NPF taking place over a large spatial area. This is because as time progresses, the particles observed at a measurement site should have originated from further and further away due to non-zero wind conditions. Following the progression of the observed NPF event and using air mass back trajectories, we can estimate where the particles observed at different stages of the NPF event were initially formed by calculating the air mass locations at the onset time of the NPF event (assuming that NPF occurs simultaneously over the larger area). Typically, the mode related to the NPF event disappears from the observations after some time. This is an indication of the currently observed air mass arriving from an area where NPF was no longer taking place due to unfavorable local conditions. If the shift in the air mass origin towards unfavorable conditions occurs gradually over time, the mode related to the NPF event can enter a stage of growth stagnation (or even decrease in size) before disappearing completely (Kivekäs et al., 2016). This is because the increasing transport time between NPF onset and observation of the particles at the measurement site provides less and less additional ‘material’ for aerosol growth towards the more unfavorable conditions. Calculating the locations where NPF is assumed to have taken place for longer data sets including several

regional NPF events can give an estimation of the typical spatial extent of NPF around the measurement location. It should be noted that even in relatively clear cases, the subjective determination of NPF event onset and end times can easily lead to uncertainties of few tens of kilometers in the estimations. In locations with strong primary pollution sources, such as urban Beijing, objective determination of NPF event start and stop times becomes even more difficult. More details and discussion related to the method and its uncertainties can be found in Kristensson et al. (2014).

2.5 NPF event classification

Particle number size distribution data from both stations were used for classifying individual days into new particle formation (NPF) event days and non-event days. This classification followed procedures presented by Dal Maso et al. (2005) and later adapted for urban locations (Chu et al., 2021) in which a day is classified as a NPF event day if (a) a new mode in the size range smaller than 25 nm appeared and (b) the new mode kept growing over several hours. On the other hand, non-event days are the days which do not fit any of the abovementioned criteria and undefined days are the days which fit either one of the abovementioned criteria. At UB site, we also observed some cases in which nucleation mode particle number concentration burst without mode diameter increase. It could be related to non-regional NPF events (Dai et al., 2017). We did not observe such cases at the MT site. Actually, the abundant anthropogenic emissions in the megacity could provide enough precursors for non-regional NPF events. However, traffic emissions can also provide abundant primary nucleation mode particles, making it difficult to distinguish whether the new mode was from NPF event or traffic. So we classified such events as "undefined" also.

2.6 Characteristics of NPF events

2.6.1 Condensation sink

The condensation sink (CS) was calculated from particle size distribution data using the method described by Kulmala et al. (2012):

$$CS = 2\pi D \sum_{dp'} \beta_{m,dp'} dp' N_{dp'} \quad (1)$$

where D is the diffusion coefficient of the condensing vapor, sulfuric acid in our case, and $\beta_{m,dp'}$ represents the transition-regime correction, $N_{dp'}$ is the particle number concentration with diameter dp'. As shown in Figure 6, particles in size range of 20-800 nm dominated the total CS at UB station and particles in the size range of 50-800 nm dominated the total CS at MT station. Although the size ranges of DMPS, FMPS and SMPS slightly differ, all of them cover the main size range which constituted the CS and thus the calculation of CS should not be significantly influenced by differences in the instrument size ranges.

As shown in Figure 6(c&e) on NPF event days, particles smaller than 100 nm built a CS of 3.7×10^{-3} s^{-1}, contributing 37% to the total CS. While at MT site, particles smaller than 100 nm only built a CS of 1.2×10^{-3} s^{-1}, contributing less than 12% to the total CS (Figure 6 (d&f)). Although 100-840 nm particle number concentration at UB site was much less than that at MT site, 1-100 nm (especially 25-100 nm) particles compensated total CS by higher number concentration on NPF event days (CS at each site will be discussed in section 3.1.2).

The data on rainy days were discarded from analysis at both sites, hence the precipitation was considered to have minor effects on our CS calculation. We calculated CS at both sites assuming RH as 0%. It should be noted that the CS may have been underestimated by a factor of 1.12-1.33 at MT site when we include RH in the CS calculation, e.g. 30%-70% during 9:00-15:00, as shown in Figure 10.

2.6.2 Particle growth rates

Growth rates were calculated for the size range of 7-15 nm ($GR_{7\text{-}15\ nm}$) using the 50% appearance time method introduced by Lehtipalo et al. (2014) and Dada et al. (2020a) according to

$$GR = \frac{dp_2 - dp_1}{t_2 - t_1} \quad (2)$$

where t_2 and t_1 are the appearance times of particles with sizes of dp_2 and dp_1, respectively. The appearance time is defined as the time at which the concentration of particles at size d_p reaches 50% of its maximum.

2.6.3 Particle formation rates

The formation rates of particles of diameters 7 nm (J_7) were calculated from particle number size distribution data using the method presented by Kulmala et al. (2012) and modified for urban environments by Cai and Jiang

(2017):

$$J_k = \frac{dN_{[d_k,d_u)}}{dt} + \sum_{d_g=d_k}^{d_{u-1}} \sum_{d_i=d_{\min}}^{+\infty} \beta_{(i,g)} N_{[d_i,d_{i+1})} - \frac{1}{2} \sum_{d_g=d_{\min}}^{d_{u-1}} \sum_{d_i^3=\max(d_{\min}^3, d_k^3-d_{\min}^3)}^{d_{i+1}^3+d_{g+1}^3 \le d_u^3} \beta_{(i,g)} N_{[d_i,d_{i+1})} N_{[d_g,d_{g+1})} + \left.\frac{dN}{dd_i}\right|_{d_i=d_u} \bullet GR_u$$

(3)

Here, J_k is the formation rate at size d_k, $cm^3 \cdot s^{-1}$, (7 nm in this study); d_u is the upper size limit of the targeted aerosol population (10 nm in this study); d_{min} is the smallest particle size detected by particle size spectrometers (to make the results comparable, the d_{min} was set to 7 nm); $N_{[dk,du)}$ is the number concentration of particles from size d_k to d_u (particles with diameters of du are not accounted for) ; d_i represents the lower limit of the i^{th} size bin; $\beta_{(i,g)}$ is the coagulation coefficient for the collision of two particles with the size of d_i and d_g; and GR_u refers to the growth rate at size d_u, $nm \cdot h^{-1}$ Deng et al. (2020b).

Determination of nucleation start and stop times was affected by traffic emissions at UB station. Hence, we chose a time window of the first 2 hours of NPF event for formation rates calculation at both sites. During the time window, we always observed 7-10 nm particle number concentration burst significantly from the background level at both sites.

3 Results and discussion

3.1 Origin of NPF events at both sites

During our observation in summer 2018 and 2019 (from June to August of each year) at UB station, there were 155 days with valid data, 53 days of which were classified as NPF event days, corresponding to an NPF event frequency of 34%. This NPF event frequency was consistent with an earlier observation in summer in urban Beijing from 2004 to 2008 while smaller than other seasons especially winter during that observation and another one-year observation in UB station (Wu et al., 2007; Wang et al., 2013;Deng et al., *2020b).*

For comparison of NPF characteristics between UB and MT stations, a parallel short-term observation was conducted at MT station from June 15 to July 14, 2019. In Figure 2, we show the particle number size distribution and CS during our short-term observations at both stations. There were a total of 12 and 13 NPF events observed at the UB station and the MT station, corresponding to an NPF event frequency of 48% (12 of

25) and 52% (13 of 25), respectively. Data were considered as valid when visual inspection of the particle number size distribution data and the instrument status did not indicate problems in the measurements. Only days with valid data at both stations were taken into consideration in our analysis. In addition, 9 NPF events were observed at both stations on the same day (referred to as common NPF events). Detailed information on the classified NPF event and non-event days, including the formation rates, growth rates, as well as their associated air mass origins during the short-term observation are provided in Table 1.

In order to understand the conditions favoring NPF events at both stations, we analyzed various ambient parameters including air mass trajectories, meteorological variables, condensation sink as well as sulfuric acid concentration.

3.1.1 Favorable air mass origin for NPF events at individual locations

In Figure 7, we show frequencies of air masses arriving at UB station from different directions during our observation in summer 2018 and 2019. The most frequent air masses arriving at UB station belonged to the South group. During our observation in the two summers, out of 155 days were 52 days belonging to the South group and 39, 32, 9 and 23 days in air masses belong to North, East, West and Local groups, respectively. NPF event frequency with respect to air masses is also shown in Figure 7. It is noticeable that air mass origin influenced the occurrence of NPF events at UB site as the majority of NPF events occurred when the air masses were coming from the north. During our observation in summer 2018 and 2019, 34 (out of 55) NPF events occurred in air masses from the North group and 9, 2, 2 and 6 NPF events in the South, East, West and Local groups, respectively (Figure 7a). One prominent feature of these air masses is their difference in CS. The CS of the air masses classified as the North group (with median values of 0.01 s^{-1} at UB station) is substantially lower than that in other air mass classes (CS = 0.03, 0.025, 0.017, 0.03 s^{-1}, for south, east, west and local, respectively), which might explain the high NPF event frequency associated with this air mass class. During the observation from June 14 to July 14 in summer 2019, the most frequent air masses arriving at both sites belonged to the North group as shown in Table 1. Out of 25 days, there were 8 and 9 days belonging to the North group, at UB and MT sites, respectively. The highest frequency of NPF events also occurred when the air masses were coming from the north. The high NPF events frequency during our observation form June 14 to July 14 could also be attributed to the frequent air masses arriving at both sites from north to Beijing.

As shown in Table 1, NPF events occurring simultaneously at both sites only happened when air masses arrived

at both sites from the same directions, suggesting that most of the observed NPF events took place over the whole studied area, extending for several hundreds of kilometers (Dai et al., 2017;Du et al., 2021). The occurrences of common NPF events also closely connected with air mass origins that 7 (out of 9) common NPF events occurred under air masses in the North group, with the other two NPF events in the South group.

3.1.2 The role of condensation sink in NPF event occurrence

Figure 8a shows the difference in CS between NPF event and non-event days during our observation in summer 2018 and 2019（two whole summers）at UB site and short-term parallel observations at both sites. The 'NPF1' and 'non-event1' referred to NPF and non-event days during the two whole summers, respectively, while 'NPF2' and 'non-event2' referred to NPF and non-event days during the short-term parallel observation period from June 14 to July 14, 2019 at both sites, respectively. The longer-term periods are used for confirming the representativeness of the short-term overlapping period for the whole summer. As shown in Figure 8a, the median CS on NPF1 or NPF2 days is equivalent for UB station (CS_{NPF1} = 0.010s^{-1}; CS_{NPF2}= 0.009s^{-1}) and less than a factor of 1.2 different between non-event1 and non-event2 in UB station ($CS_{nonevent1}$ = 0.023s^{-1}; $CS_{nonevent2}$= 0.020s^{-1}), which confirms the representativeness of our short-term measurement period to the overall urban Beijing summer.

Our results in Figure 8a show that the median CS was ~ 0.01 s^{-1} during the first 2 hours of the NPF events, at both stations. On common NPF event days, the median CS was 0.009 s^{-1} at UB station and ~0.01s^{-1} at MT station, respectively. In comparison, on non-event days, during roughly the same time period (9:00–11:00 LT), the CS was substantially higher, with median values of 0.02 s^{-1} and 0.014 s^{-1}, at UB and MT stations, respectively. Figure 8b presents the median CS during the first 2 hours of NPF events on common NPF event days measured at both stations, and shows the high correlation between the two.

Figure 8c shows the NPF event frequency as a function of CS during our observation at UB site in summer 2018 and 2019 and how the NPF event frequency decreased with increasing CS. When CS was smaller than 0.01 s^{-1}, all days were classified as NPF event days, and when CS was larger than 0.035 s^{-1}, no day was classified as NPF event day. This shows the major role of background particles in controlling the occurrence or inhibition of NPF events as shown in several previous studies in China and internationally (Deng et al., 2020a; Cai et al., 2017; Kulmala et al., 2017). While we cannot present a similar figure from the MT station, the same conclusion applies where CS does play a role in inhibiting NPF observation owing to the difference in the CS values

observed between NPF and nonevents at MT as shown in figure 8a. Yet, since the overall preexisting particle concentration at the MT is rather on the low end, the role of CS might not be as vital at the MT station as for the UB station.

Different from NPF events under low CS (<0.01 s^{-1}), these NPF events under high CS were characterized by a relatively high H_2SO_4 concentration (>10^7 cm^{-3}) or low formation rates (Figure 9a), discussed in further details in the coming sections. In comparison, at MT station, when CS was smaller than ~ 0.013 s^{-1}, most (10 out of 14) days were classified as NPF event days as shown in Figure 9d. When CS was larger than ~0.013 s^{-1}, we only observed one local NPF event and another two non-local NPF events (Table 1). The local NPF event under high CS at the MT station was characterized as high UV (>30 W/m^2) and low formation rate (J_7 were too small to be reliably calculated) as well.

3.1.3 Role of meteorological variables in NPF event occurrence

While the air mass source regions, and their connection to the CS, seem to explain the general picture of NPF event occurrences at the two sites well, we still have some cases unexplained. For example, as shown in Table 1, there were several non-event days observed at MT station with air masses belonging to North and West groups, which were connected to low CS. This indicates that a further investigation into other NPF-related variables is still required.

In Figure 10, we show diurnal variation of meteorological variables during our observation in summer 2018 and 2019 at UB site and observations from June 14 to July 14 in 2019 at UB and MT sites. It is noticeable that the short-term observation compared well with the long-term observation and therefore is representative of summer at UB site as shown in Figure 10.

First, the intensity of solar radiation is considered to be one of the most important parameters deciding NPF event occurrence as it translates into photochemistry strength (Chu et al., 2019). The median UV (UVA+UVB) intensity at the UB station on NPF event and non-event days was 38.3 and 32.9 W/m^2, respectively. The UV intensity was on average ~15% higher on NPF event days than on non-event days at UB station. Although UV intensity was important for NPF event occurrence, we still observed NPF events at UB station under low UV intensity, e.g. cases on June 30 and July 6. These two events all started immediately after sunrise (6:30 LT on June 30 and 7:00 LT on July 6, see Table 1) and median UV intensity during the first two hours of NPF events was only 13.2 and 14.1 W/m^2, respectively. However, sulfuric acid concentration was higher than 10^7 cm^{-3} at the

same time, the possible reason is high SO_2 concentration and low CS (~0.003 s^{-1}) outcompeted the low UV intensity (Dada et al., 2020b) as well as the possibility of having other H_2SO_4 sources (Yao et al., 2020).

At MT station, the median UV intensity on NPF event and non-event days was 28.4 and 14.2 W/m^2, respectively. The lower UV at MT station, in general might be related to the higher RH (Figure 10c&d) and thus more cloudiness and fog at the MT station (Hamed et al., 2010;Dada et al., 2018). The UV intensity was on average ~100% higher on NPF event days than on non-event days at UB station. All local NPF events happened when UV intensity was higher than 15 W/m^2 as shown in Figure 9d.

On the other hand, as shown in Figure 10c&d, the median relative humidity (RH) was lower on NPF event days than non-event days at both stations. This is consistent with earlier results that high RH suppressed NPF events by increasing CS and coagulation sink (CoagS), as it can enhance the particle hygroscopic growth (Hamed et al., 2010; Hamed et al., 2011). In addition, high RH was also found to be associated with more clouds resulting in less solar radiation (Dada et al., 2018).

The median temperatures at UB on event and non-event days were 31 ℃ and 29 ℃, respectively, and at MT station 23 ℃ and 19 ℃, respectively. The median temperature was lower at the MT station than at the UB station, due to the higher altitude of the station and likely also the weaker solar radiation (Figure 10e&f). At both stations, the median temperature was very similar on NPF event and non-event days, suggesting that temperature was not a crucial factor for NPF event occurrence during the measurement in summer.

3.1.4 Role of sulfuric acid concentrations in NPF event occurrence

Sulfuric acid has been found to be the main precursor vapor participating in NPF in China and in many locations around the world due to its low volatility (Yao et al., 2018;Chu et al., 2019). In Figure 9a, we show the concentration of sulfuric acid as a function of CS during summer 2018 and 2019 at UB site. As shown in Figure 9b, the median sulfuric acid (H_2SO_4) concentrations at UB station were 8.1×10^6 cm^{-3} and 4.5×10^6 cm^{-3} on NPF event days and non-event days, respectively, during observation from June 14 to July 14 in 2019 and 7.9×10^6 cm^{-3} and 3.4×10^6 cm^{-3} on NPF event days and non-event days, respectively, during the observation in summer 2018 and 2019. This suggests that H_2SO_4 was important for NPF events at the UB station (Deng et al., 2020b; Dada et al., 2020b). On the other hand, as shown in Figure 9a, the H_2SO_4 concentration during 9:00- 11:00 (local time) on non-event days could be comparable with that on NPF event days, especially when CS was high. The H_2SO_4 concentration during 9:00- 11:00 (local time) on non-event days could be comparable with that on NPF

406 event days, especially when CS was high. Altogether, our observation shows that the occurrence of NPF events
407 was controlled by both H_2SO_4 and CS at the UB station (Cai et al., 2020).
408 In addition, although we did not perform the measurement of H_2SO_4 at the MT station, concentration of H_2SO_4
409 is expected to be much lower than that at the UB station. First, the SO_2 concentration at measurement at
410 Longquan Town was always below the detection limit (~ 0.5 ppb) during our observation period. In comparison,
411 median SO_2 concentration at UB station was 0.87 ppb for all days and 0.65 ppb for NPF event days during our
412 short-term parallel observation period. The spatial decreasing trend of SO_2 concentration from urban Beijing to
413 the west implies a low SO_2 concentration at the MT station, especially when the nearby anthropogenic sources
414 are sparse (Liu, 2008; Ying, 2010;Wang, 2011;Yang-Chun et al., 2013). Second, the oxidation of SO_2 by
415 photochemistry reactions could also be limited by the low solar radiation at the MT station as we discussed in
416 3.1.3. Third, CS, as the main sink of H_2SO_4, was comparable at the MT station to that in the UB station on NPF
417 event days (as shown in Figure 8a). Altogether, the lower production rate and the equivalent loss rate of H_2SO_4
418 at the MT station likely result in the lower H_2SO_4 concentration, in comparison to UB station.
419 Due to the lack of H_2SO_4 measurements, the NPF mechanism at the MT station cannot be inferred. Nevertheless,
420 we show that the occurrence of NPF is a response to photochemistry (and very likely to H_2SO_4) and CS in
421 Figure 9d. It is clear that high UV intensity and low CS favored the occurrence of NPF. However, there existed
422 exceptions. For example, two NPF events were observed even when the UV intensity was low and the CS was
423 high, besides, it was an undefined day on June 28 despite of the high UV intensity and low CS. These
424 exceptional cases will be discussed in detail in Section 3.6.1 and 3.6.2, respectively.

425 ***3.2 NPF event start time at both stations***

426 There was no significant difference in NPF event start times between the long-term and short-term parallel
427 observations at UB site. In this section, we only compare NPF event start times of coincident events at UB and
428 MT sites during the short-term parallel observations.
429 During our observation, there was no advection of air masses between the two sites on common NPF event days,
430 indicating that the NPF events occurred at each site independently. As shown in Table 1, all common NPF
431 events started after sunrise and prior to noon except the two non-local NPF events at MT station. However, NPF
432 event start time was different between the two sites. Earlier researches in Nanjing, China and Nordic stations

showed the similar results that NPF events can be observed simultaneously at two or more sites, but the start time can be different, local meteorology, source strength and background aerosols could drive temporal behavior of NPF events at each sites (Hussein et al., 2009;Dai et al., 2017).

3.3 Particle formation and growth rates at both stations

The formation rates (J_7) at the two stations during the measurements are presented in Figure 11a. J_7 observed during the short-term parallel observation (NPF2) at UB site were in the range of 3.0-10.0 cm^{-3} s^{-1} with a median of 5.4 cm^{-3} s^{-1}, comparable with those observed in summer 2018 and 2019 (NPF1 = 2-14.0 cm^{-3} s^{-1} with a median of 4.9 cm^{-3} s^{-1}) and significantly higher than the values in the MT station (0.75-3.0 cm^{-3} s^{-1} with a median of 0.82 $cm^{-3}s^{-1}$) for common NPF events (Figure 11b). These values are comparable to earlier observations in urban Beijing and another regional background station in North China Plain (NCP) (Wang et al., 2013). Earlier observations in NCP and Yangtze River Plain also show higher formation rates at urban sites than corresponding background sites by roughly a factor of 2 due to lower anthropogenic emissions at background sites (Wang et al., 2013;Dai et al., 2017;Shen et al., 2018). The much lower J_7 observed at MT station is very likely associated with the low H_2SO_4 concentration at this station, as we discussed above. However, other reasons, such as the low concentration of H_2SO_4 stabilizers, e.g., amines, cannot be ruled out either. Also, the J_7 at UB station could be affected by particle emissions due to the proximity of the location to the highway, while compared with NPF events, the effect of traffic emissions is shown to be minor (Kontkanen et al., 2020; Zhou at al., 2020). In addition, Boulon et al. (2011) observed that new particles could be formed at low altitude and transported to the higher altitude sites, however, to confirm whether the phenomenon can happen at MT site, we still need observation on vertical wind conditions or vertical evolution of potential temperature.

The growth rates in size range of 7-15 nm ($GR_{7\text{-}15nm}$) at the UB station (4.8-12.9 nm/h with a median of 7.8 nm/h) during NPF2 was also comparable with the whole summers (NPF1) (4.8-12.9 nm/h with a median of 8.5 nm/h). While the difference in J_7 was 7 times higher in UB than in MT, the observed GR were only a slightly higher at UB than at the MT station (5.7-10.5 nm/h with a median of 6.5 nm/h) for common NPF events (Figure 11c&d), implying that precursors needed for particle formation were much more abundant in the polluted urban environment (Wang et al., 2013), while those needed for growth are rather comparable. The GR at UB station was comparable to other long-term observation at UB station (1.1-8.0 nm/h) in 2018, and other urban areas in

China (Herrmann et al., 2014;Chu et al., 2019;Deng et al., 2020b). Consistent with earlier observations showing that H_2SO_4 could only contribute to a small fraction of the particle growth in this size range (Paasonen et al., 2018;Qi et al., 2018;Guo et al., 2020), the growth rates at both stations cannot be explained by the H_2SO_4 concentration. This implies that other condensable species, very likely low-volatility organic vapors, play an important role in particle growth at both stations. At the UB station, anthropogenic VOCs are dominant precursors of these low-volatility organic vapors (Guo et al., 2020; Deng et al., 2020a), while VOCs at MT station, with rare anthropogenic sources, are likely dominated by biogenic emissions.

3.4 Ending diameters of newly-formed grown particles

Earlier observations have shown that diameters of newly-formed particles should be larger than 70 nm to contribute to cloud condensation nuclei significantly (Man et al., 2015; Ma et al., 2021) and will be considered as haze particles when their size reaches larger than 100 nm (Kulmala et al., 2021). In Figure 12, we show ending diameters (End Dp) of newly formed grown particles during our observations at both sites. End Dp during the observation from June 14 to July 14 at UB site (21-105 nm, with a median of 49 nm, Figure 12a) had similar characteristics as those during the long-term observation in summer (21-126 nm, with a median of 56 nm, Figure 12a) where most of End Dp were in the range of 25-70 nm. As shown in Fig.12b, 61% of End Dp were in the range of 25-70 nm, and only 9% of End Dp were larger than 100 nm during our observation in summer 2018 and 2019 at UB site. We found that the ending diameters slightly higher at UB site than MT site, but the difference is not significant (49 nm vs 45 nm) as shown in Figure 12c.

Earlier research has pointed out that in order to observe particle growth until 100 nm at a measurement station under typical conditions, simultaneous NPF should happen over a very large area (e.g. with wind speed 5 m/s and growth rate of 3 nm/h from the station to roughly 600 km upwind from the station) (Paasonen et al., 2018). During our observation in summer 2018 and 2019, most of the newly formed modes kept growing for about 20 hours after an NPF event started, and the maximum horizontal extension of the observed NPF events in the growth stage is restricted to within about 200 km (~2° in latitude) north of UB site (Figure 13). As shown in Figure 13, the population density is also higher within the area extending ~200 km north than beyond this limit. Therefore, it seems that NPF events were limited to the regions with some contribution from anthropogenic emissions during air mass transport from north to Beijing. Roughly similar extent of the NPF area is also seen in

other directions. However, towards the south it is more likely that increasing condensation sink from accumulating pollution becomes the limiting factor for NPF occurrence rather than decreasing strength in emission sources. NPF events at MT station had similar characteristics as those at UB station with the NPF event region extending a few hundred kilometers towards the north. The NPF events in this direction were disrupted after a relatively similar distance (or they enter the growth stagnation phase). The limited NPF event area could possibly explain why most End Dp we observed were smaller than 70 nm.

3.5 Effect of topography

In Figure 14, we show average particle number size distributions and particle number concentrations on NPF event and non-event days during our short-term parallel observation at both sites. On NPF event days, nucleation (6-25 nm) and Aitken (25-100 nm) mode particle number concentrations were much smaller at MT station than those at UB station due to smaller formation rates and less anthropogenic emissions. Interestingly, accumulation (100-840 nm) mode particle number concentrations were higher at MT station (701-2900 cm^{-3}, with a median of 1500 cm^{-3}) than those at UB station (350-1416 cm^{-3} with a median of 700 cm^{-3}) (Figure 14b). Due to the close proximity of the two measurement sites, the air mass arrival directions and source regions were (mostly) similar at both sites throughout the measurement period, hence the regional and transported air masses cannot explain the higher accumulation mode particle number concentration at MT site. As there were few primary emissions at MT site, the accumulation mode particles could be attributed to secondary particles (Kulmala et al., 2021), indicating particles at MT station were more aged than those at UB station (Figure 14a). The possible reasons is that mountains block pollution diffusion, which in the end resulted in comparable CS at MT station as UB station.

Figure 15 shows an example of the wind distribution before and during NPF event on June 30, 2019 at 850 hPa (close to the altitude of MT station) and 10 m above ground level. As shown in Figure 15, the reanalyzed wind directions at 850 hPa were similar as those at 10 m above the ground level at MT station. Actually, the wind conditions on other NPF event days at MT station during our observation had similar characteristics that the wind directions were similar between 850 hPa and 10 m above ground level indicating air masses well mixed during NPF events. Earlier observations also found NPF event happened uniformly within the mixing layer at their observation stations and particle number size distribution remains roughly constant within the mixing layer

514 (Shen et al., 2018;Lampilahti et al., 2021).

515 **4 Summary and conclusions**

516 We conducted observations of NPF events at an urban site (UB) and a background mountain site (MT) in
517 Beijing and fully analyzed the favorable conditions for NPF event occurrences at each of the sites. In order to
518 identify the similarities and differences between NPF events at both stations in terms of frequency, intensity, we
519 compared certain NPF events' characteristics including formation rate, growth rate as well as NPF event start
520 time and ending diameters of newly-formed growing particles at both stations. We found that NPF events are
521 most of the time a regional phenomenon occurring over the studied areas and connected closely with air masses
522 source regions during our observation. The air masses from north favored common NPF events more than any
523 other mass trajectories due to their associated clean air masses and thus low CS. Additionally, air masses from
524 the north group always resulted in an NPF event at UB station, while other factors still suppressed their
525 occurrence at the MT station. For example, we found that sufficiently high solar radiation, e.g. UV (UVA+UVB)
526 intensity larger than 15 W/m^2 is required for an NPF event to occur at MT and NPF events observed under solar
527 radiation conditions smaller than 15 W/m^2 were rather transported NPF events from areas upwind to MT station.
528 Moreover, we found that the CS limit for NPF event occurrence at UB station was ~0.032 s^{-1}, which is
529 consistent with earlier observations in urban Beijing. In comparison, at MT station the CS limit could be
530 ~0.013 s^{-1}, above which local-NPF events could possibly be suppressed associated with the lower SO_2
531 concentration.

532 Although NPF events could happen simultaneously at both stations, the NPF event strength (formation rates)
533 was significantly higher at UB than MT station, possibly due to spatial inhomogeneity in the sources of aerosol
534 precursor compounds as well as solar radiation. In addition, the growth rates in size range of 7-15 nm were also
535 slightly higher at UB than MT station. Regional NPF events were observed to occur with the horizontal extent
536 within around 200 kilometers when air masses arriving at Beijing from the north, as a result, only a few NPF
537 events were observed to end with mode diameters larger than 70 nm. The upwind extension of regional NPF
538 events was limited to the areas with some anthropogenic emissions. There should not be any discrete boundary
539 between the regions that NPF event is or is not occurring, but with decreasing anthropogenic emissions, the
540 strength (formation rates and growth rates) should decrease. Overall, our results highlight the importance of
541 anthropogenic emissions for NPF events occurrence and subsequently growth in north China plain during

summer. However, there are still some uncertainties due to the limited data set. For more robust knowledge on NPF events in north China plain, and to figure out the effect of urban emissions on regional NPF events, we still need long-term observation including particle number size distribution down to sub-3 nm, gas and particle phase chemistry upwind and downwind urban Beijing. Such observations can shed light into the regionality of NPF events and the dynamical development of the aerosol population influenced by radical chemistry in the plume of a megacity.

Conflict of interest: The authors declare no competing interests.

Author contributions: YZ, CY, YG, XY performed the measurements. YZ, SH, CY, YG, LD, XY analyzed the data. YZ, CY, SH, LD wrote the manuscript. All authors reviewed the paper and contributed to the scientific discussions.

Data availability: The data displayed in this manuscript will be available online at zenodo.com once the manuscript is in its final publication format.

Financial support: This publication has been produced within the framework of the EMME-CARE project, which has received funding from the European Union's Horizon 2020 Research and Innovation Programme (under grant agreement no. 856612) and the Government of Cyprus. This research has also received funding from the European Commission grant agreement no. 742206 ("ERC-ATM-GTP") as well as Academy of Finland Projects 316114 & 311932. Simo Hakala acknowledges the doctoral programme in Atmospheric Sciences (ATM-DP, University of Helsinki) for financial support. The sole responsibility of this publication lies with the author. The European Union is not responsible for any use that may be made of the information contained therein.

5 References

Boulon, J., Sellegri, K., Hervo, M., Picard, D., Pichon, J.-M., Fréville, P., and Laj, P.: Investigation of nucleation events vertical extent: a long term study at two different altitude sites, Atmos. Chem. Phys., 11, 5625–5639, https://doi.org/10.5194/acp-11-5625-2011, 2011.

Cai, R., and Jiang, J.: A new balance formula to estimate new particle formation rate: reevaluating the effect of coagulation scavenging, Atmos Chem Phys, 17, 12659-12675, 10.5194/acp-17-12659-2017, 2017.

Cai, R., Yang, D., Fu, Y., Wang, X., Li, X., Ma, Y., Hao, J., Zheng, J., and Jiang, J.: Aerosol surface area concentration: a governing factor in new particle formation in Beijing, Atmos Chem Phys, 17, 12327-12340, 10.5194/acp-17-12327-2017, 2017.

Cai, R., Yan, C., Yang, D., Yin, R., Lu, Y., Deng, C., Fu, Y., Ruan, J., Li, X., Kontkanen, J., Zhang, Q., Kangasluoma, J., Ma, Y., Hao, J., Worsnop, D. R., Bianchi, F., Paasonen, P., Kerminen, V.-M., Liu, Y., Wang, L., Zheng, J., Kulmala, M., and Jiang, J.: Sulfuric acid-amine nucleation in urban Beijing, Atmospheric Chemistry and Physics Discussions, 10.5194/acp-2020-1060, 2020.

Carnerero, C., Pérez, N., Reche, C., Ealo, M., Titos, G., Lee, H.-K., Eun, H.-R., Park, Y.-H., Dada, L., Paasonen, P., Kerminen, V.-M., Mantilla, E., Escudero, M., Gómez-Moreno, F. J., Alonso-Blanco, E., Coz, E., Saiz-Lopez, A., Temime-Roussel, B., Marchand, N., Beddows, D. C. S., Harrison, R. M., Petäjä, T., Kulmala, M., Ahn, K.-H., Alastuey, A., and Querol, X.: Vertical and horizontal distribution of regional new particle formation events in Madrid, Atmos Chem Phys, 18, 16601-16618, 10.5194/acp-18-16601-2018, 2018.

Casquero-Vera, J. A., Lyamani, H., Dada, L., Hakala, S., Paasonen, P., Román, R., Fraile, R., Petäjä, T., Olmo-Reyes, F. J., and Alados-Arboledas, L.: New particle formation at urban and high-altitude remote sites in the south-eastern Iberian Peninsula, Atmos. Chem. Phys., 20, 14253–14271, https://doi.org/10.5194/acp-20-14253-2020, 2020.

Chu, B., Dada, L., Liu, Y., Yao, L., Wang, Y., Du, W., Cai, J., Daellenbach, K., Chen, X., Simonen, P., Zhou, Y., Deng, C., Fu, Y., Yin, R., Li, H., He, X.-C., Feng, Z., Yan, C., Kangasluoma, J., and Kulmala, M.: Particle growth with photochemical age from new particle formation to haze in the winter of Beijing, China, Science of The Total Environment., 753, 10.1016/j.scitotenv.2020.142207, 2021.

Chu, B. W., Kerminen, V. M., Bianchi, F., Yan, C., Petäjä, T., and Kulmala, M.: Atmospheric new particle

591 formation in China, Atmos Chem Phys, 19, 115-138, https://doi.org/10.5194/acp-19-115-2019, 2019.
592 Dada, L., Paasonen, P., Nieminen, T., Buenrostro Mazon, S., Kontkanen, J., Peräkylä, O., Lehtipalo, K., Hussein,
593 T., Petäjä, T., Kerminen, V.-M., Bäck, J., and Kulmala, M.: Long-term analysis of clear-sky new particle
594 formation events and nonevents in Hyytiälä, Atmos Chem Phys, 17, 6227-6241, 10.5194/acp-17-6227-2017,
595 2017.
596 Dada, L., Chellapermal, R., Buenrostro Mazon, S., Paasonen, P., Lampilahti, J., Manninen, H. E., Junninen, H.,
597 Petäjä, T., Kerminen, V.-M., and Kulmala, M.: Refined classification and characterization of atmospheric
598 new-particle formation events using air ions, Atmos Chem Phys, 18, 17883-17893, 10.5194/acp-18-17883-2018,
599 2018.
600 Dada, L., Lehtipalo, K., Kontkanen, J., Nieminen, T., Baalbaki, R., Ahonen, L., Duplissy, J., Yan, C., Chu, B.,
601 Petäjä, T., Lehtinen, K., Kerminen, V.-M., Kulmala, M., and Kangasluoma, J.: Formation and growth of
602 sub-3-nm aerosol particles in experimental chambers, Nat Protoc, , 15, 1013-1040, 10.1038/s41596-019-0274-z,
603 2020a.
604 Dada, L., Ylivinkka, I., Baalbaki, R., Li, C., Guo, Y., Yan, C., Yao, L., Sarnela, N., Jokinen, T., Daellenbach, K.
605 R., Yin, R., Deng, C., Chu, B., Nieminen, T., Kontkanen, J., Stolzenburg, D., Sipilä, M., Hussein, T., Paasonen,
606 P., Bianchi, F., Salma, I., Weidinger, T., Pikridas, M., Sciare, J., Jiang, J., Liu, Y., Petäjä, T., Kerminen, V.-M.,
607 and Kulmala, M.: Sources and sinks driving sulphuric acid concentrations in contrasting environments:
608 implications on proxy calculations, Atmos. Chem. Phys. Discuss., 10.5194/acp-2020-155, 2020b.
609 Dai, L., Wang, H., Zhou, L., An, J., Tang, L., Lu, C., Yan, W., Liu, R., Kong, S., Chen, M., Lee, S., and Yu, H.:
610 Regional and local new particle formation events observed in the Yangtze River Delta region, China, Journal of
611 Geophysical Research: Atmospheres, 122, 2389-2402, 10.1002/2016jd026030, 2017.
612 Dal Maso, M., Kulmala, M., Riipinen, I., Wagner, R., Hussein, T., Aalto, P. P., and Lehtinen, K. E. J.: Formation
613 and growth of fresh atmospheric aerosols: eight years of aerosol size distribution data from SMEAR II, Hyytiala,
614 Finland, Boreal Environ Res, 10, 323-336, 2005.
615 Deng, C., Cai, R., Yan, C., Zheng, J., and Jiang, J.: Formation and growth of sub-3 nm particles in megacities:
616 impact of background aerosols, Faraday Discuss, 10.1039/d0fd00083c, 2020a.
617 Deng, C., Fu, Y., Dada, L., Yan, C., Cai, R., Yang, D., Zhou, Y., Yin, R., Lu, Y., Li, X., Qiao, X., Fan, X., Nie, W.,
618 Kontkanen, J., Kangasluoma, J., Chu, B., Ding, A., Kerminen, V. M., Paasonen, P., Worsnop, D. R., Bianchi, F.,

Liu, Y., Zheng, J., Wang, L., Kulmala, M., and Jiang, J.: Seasonal Characteristics of New Particle Formation and Growth in Urban Beijing, Environ Sci Technol, 54, 8547-8557, 10.1021/acs.est.0c00808, 2020b.

Du, W., Dada, L., Zhao, J., Chen, X., Daellenbach, K. R., Xie, C., Wang, W., He, Y., Cai, J., Yao, L., Zhang, Y., Wang, Q., Xu, W., Wang, Y., Tang, G., Cheng, X., Kokkonen, T. V., Zhou, W., Yan, C., Chu, B., Zha, Q., Hakala, S., Kurppa, M., Järvi, L., Liu, Y., Li, Z., Ge, M., Fu, P., Nie, W., Bianchi, F., Petäjä, T., Paasonen, P., Wang, Z., Worsnop, D. R., Kerminen, V.-M., Kulmala, M., and Sun, Y.: A 3D study on the amplification of regional haze and particle growth by local emissions, npj Climate and Atmospheric Science, 4, 10.1038/s41612-020-00156-5, 2021.

Ehn, M., Thornton, J.A., Kleist, E., Sipila, M., Junninen, H., Pullinen, I., Springer, M., Rubach, F., Tillmann, R., Lee, B., Lopez-Hilfiker, F., Andres, S., Acir, I.-H., Rissanen, M., Jokinen, T., Schobesberger, S., Kangasluoma, J., Kontkanen, J., Nieminen, T., Kurten, T., Nielsen, L. B., Jorgensen, S., Kjaergaard, H. G., Canagaratna, M., Maso, M. D., Berndt, T., Petaja, T., Wahner, A., Kerminen, V.-M., Kulmala, M., Worsnop, D. R., Wildt, J., and Mentel, T. F.: A large source of low-volatility secondary organic aerosol, Nature, 506, 476–479., 2014.

Gao, Y., Zhang, D., Wang, J., Gao, H., and Yao, X.: Variations in Ncn and Nccn over China marginal seas related to marine traffic emissions, new particle formation and aerosol aging, Atmos. Chem. Phys., in press 2020.

Guo, S., Hu, M., Zamora, M. L., Peng, J. F., Shang, D. J., Zheng, J., Du, Z. F., Wu, Z., Shao, M., Zeng, L. M., Molina, M. J., and Zhang, R. Y.: Elucidating severe urban haze formation in China, P Natl Acad Sci USA, 111, 17373-17378, 10.1073/pnas.1419604111, 2014.

Guo, S., Hu, M., Peng, J., Wu, Z., Zamora, M. L., Shang, D., Du, Z., Zheng, J., Fang, X., Tang, R., Wu, Y., Zeng, L., Shuai, S., Zhang, W., Wang, Y., Ji, Y., Li, Y., Zhang, A. L., Wang, W., Zhang, F., Zhao, J., Gong, X., Wang, C., Molina, M. J., and Zhang, R.: Remarkable nucleation and growth of ultrafine particles from vehicular exhaust, Proc Natl Acad Sci U S A, 117, 3427-3432, 10.1073/pnas.1916366117, 2020.

Hakala, S., Alghamdi, M. A., Paasonen, P., Vakkari, V., Khoder, M. I., Neitola, K., Dada, L., Abdelmaksoud, A. S., Al-Jeelani, H., Shabbaj, I. I., Almehmadi, F. M., Sundström, A.-M., Lihavainen, H., Kerminen, V.-M., Kontkanen, J., Kulmala, M., Hussein, T., and Hyvärinen, A.-P.: New particle formation, growth and apparent shrinkage at a rural background site in western Saudi Arabia, Atmos Chem Phys, 19, 19, https://doi.org/10.5194/acp-19-10537-2019, 2019.

Hamed, A., Korhonen, H., Sihto, S.-L., Joutsensaari, J., Järvinen, H., Petäjä, T., Arnold, F., Nieminen, T., Kulmala, M., Smith, J. N., Lehtinen, K. E. J., Laaksonen, A., and High relative humidity supresses contenental new particle formation events, 2010.

Hamed, A., Korhonen, H., Sihto, S.-L., Joutsensaari, J., Järvinen, H., Petäjä, T., Arnold, F., Nieminen, T., Kulmala, M., Smith, J. N., Lehtinen, K. E. J., and Laaksonen, A.: The role of relative humidity in continental new particle formation, Journal of Geophysical Research, 116, 10.1029/2010jd014186, 2011.

Herrmann, E., Ding, A. J., Kerminen, V. M., Petäjä, T., Yang, X. Q., Sun, J. N., Qi, X. M., Manninen, H., Hakala, J., Nieminen, T., Aalto, P. P., Kulmala, M., and Fu, C. B.: Aerosols and nucleation in eastern China: first insights from the new SORPES-NJU station, Atmos Chem Phys, 14, 2169-2183, 10.5194/acp-14-2169-2014, 2014.

Hussein, T., Junninen, H., Tunved, P., Kristensson, A., Dal Maso, M., Riipinen, I., Aalto, P. P., Hansson, H. C., Swietlicki, E., and Kulmala, M.: Time span and spatial scale of regional new particle formation events over Finland and Southern Sweden, Atmos Chem Phys, 9, 4699-4716, 10.5194/acp-9-4699-2009, 2009.

Jun, Y.-S., Jeong, C.-H., Sabaliauskas, K., Richard Leaitch, W., and Evans, G. J.: A year-long comparison of particle formation events at paired urban and rural locations, Atmospheric Pollution Research, 5, 447-454, 10.5094/apr.2014.052, 2014.

Kangasluoma, J., Cai, R., Jiang, J., Deng, C., Stolzenburg, D., Ahonen, L. R., Chan, T., Fu, Y., Kim, C., Laurila, T. M., Zhou, Y., Dada, L., Sulo, J., Flagan, R. C., Kulmala, M., Petäjä, T., and Lehtipalo, K.: Overview of measurements and current instrumentation for 1–10 nm aerosol particle number size distributions, J Aerosol Sci, 148, 10.1016/j.jaerosci.2020.105584, 2020.

Kerminen, V. M., Chen, X. M., Vakkari, V., Petäjä, T., Kulmala, M., and Bianchi, F.: Atmospheric new particle formation and growth: review of field observations, Environ Res Lett, 13, https://doi.org/10.1088/1748-9326/aadf3c, 2018.

Komppula, M., Lihavainen, H., Hatakka, J., Paatero, J., Aalto, P., Kulmala, M., and Viisanen, Y.: Observations of new particle formation and size distributions at two different heights and surroundings in subarctic area in northern Finland, J. Geophys. Res.-Atmos., 108, 4295, https://doi.org/10.1029/2002jd002939, 2003.

Komppula, M., Sihto, S.-L., Korhonen, H., Lihavainen, H., Kerminen, V.-M., Kulmala, M., and Viisanen, Y.: New particle formation in air mass transported between two measurement sites in Northern Finland, Atmos Chem Phys, 6, 14, www.atmos-chem-phys.net/6/2811/2006/, 2006.

675 Kontkanen, J., Deng, C., and Fu, Y., Dada, L., Zhou, Y., Cai, J., Daellenbach, R.-K., Hakala, S., Kokkonen,
676 V.-T., Lin, Z., Liu, Y., Wang, Y., Yan, C., Petäjä, T., Jiang, J., Kulmala, M and Paasonen, P.: Size-resolved
677 particle number emissions in Beijing determined from measured particle size distributions, Atmos Chem Phys,
678 20, 11329–11348, https://doi.org/10.5194/acp-20-11329-2020, 2020.
679 Kivekäs, N., Carpman, J., Roldin, P., Leppä, J., O'Connor, E., Kristensson, A., and Asmi, E.: Coupling an
680 aerosol box model with one-dimensional flow: a tool for understanding observations of new particle formation
681 events, Tellus B, 68, 29706, doi:10.3402/tellusb.v68.29706, 2016.
682 Kristensson, A., Johansson, M., Swietlicki, E., Kivekäs, N., Hussein, T., Nieminen, T., Kulmala, M., and Dal
683 Maso, M.: NanoMap: geographical mapping of atmospheric new particle formation through analysis of particle
684 number size distribution data, Boreal Environ. Res., 19 (suppl. B), 329—342, 2014.
685 Kulmala, M., Petäjä, T., Nieminen, T., Sipilä, M., Manninen, H. E., Lehtipalo, K., Dal Maso, M., Aalto, P. P.,
686 Junninen, H., Paasonen, P., Riipinen, I., Lehtinen, K. E. J., Laaksonen, A., and Kerminen, V. M.: Measurement
687 of the nucleation of atmospheric aerosol particles, Nat Protoc, 7, 1651-1667,
688 https://doi.org/10.1038/nprot.2012.091, 2012.
689 Kulmala, M., Dada, L., Dällenbach, K., Yan, C., Stolzenburg, D., Kontkanen, J., Ezhova, E., Hakala, S.,
690 Tuovinen, S., Kokkonen, T., Kurppa, M., Cai, R., Zhou, Y., Yin, R., Baalbaki, R., Chan, T., Chu, B., Deng, C.,
691 Fu, Y., Ge, M., He, H., Heikkinen, L., Junninen, H., Nei, W., Rusanen, A., Vakkari, V., Wang, Y., Wang, L., yao,
692 l., Zheng, J., Kujansuu, J., Kangasluoma, J., Petäjä, T., Paasonen, P., Järvi, L., Worsnop, D., Ding, A., Liu, Y.,
693 Jiang, J., Bianchi, F., Yang, G., Liu, Y., Lu, Y., and Kerminen, V.-M.: Is reducing new particle formation a
694 plausible solution to mitigate particulate air pollution in Beijing and other Chinese megacities?, Faraday Discuss,
695 10.1039/d0fd00078g, 2021.
696 Lampilahti, J., Manninen, H. E., Nieminen, T., Mirme, S., Ehn, M., Pullinen, I., Leino, K., Schobesberger, S.,
697 Kangasluoma, J., Kontkanen, J., Järvinen, E., Väänänen, R., Yli-Juuti, T., Krejci, R., Lehtipalo, K., Levula, J.,
698 Mirme, A., Decesari, S., Tillmann, R., Worsnop, D. R., Rohrer, F., Kiendler-Scharr, A., Petäjä, T., Kerminen,
699 V.-M., Mentel, T. F., and Kulmala, M.: Zeppelin-led study on the onset of new particle formation in the
700 planetary boundary layer, Atmospheric Chemistry and Physics Discussions, 10.5194/acp-2021-282, 2021.
701 Lehtipalo, K., Leppä, J., Kontkanen, J., Kangasluoma, J., Wimmer, D., Franchin, A., Schobesberger, S.,
702 Junninen, H., Petäjä, T., Sipilä, M., Mikkilä, J., Vanhanen, J., Worsnop, D. r., and Kulmala, M.: methods for

703 determining particle size distribution and growth rates between 1 and 3 nm using the Particle Size Magnifier,
704 Boreal Environ Res, 19 215-236, 2014.
705 Lehtipalo, K., Yan, C., Dada, L., Bianchi, F., Xiao, M., Wagner, R., Stolzenburg, D., Ahonen, L. R., Amorim, A.,
706 Baccarini, A., Bauer, P. S., Baumgartner, B., Bergen, A., Bernhammer, A. K., Breitenlechner, M., Brilke, S.,
707 Buchholz, A., Mazon, S. B., Chen, D. X., Chen, X. M., Dias, A., Dommen, J., Draper, D. C., Duplissy, J., Ehn,
708 M., Finkenzeller, H., Fischer, L., Frege, C., Fuchs, C., Garmash, O., Gordon, H., Hakala, J., He, X. C.,
709 Heikkinen, L., Heinritzi, M., Helm, J. C., Hofbauer, V., Hoyle, C. R., Jokinen, T., Kangasluoma, J., Kerminen, V.
710 M., Kim, C., Kirkby, J., Kontkanen, J., Kurten, A., Lawler, M. J., Mai, H. J., Mathot, S., Mauldin, R. L., Molteni,
711 U., Nichman, L., Nie, W., Nieminen, T., Ojdanic, A., Onnela, A., Passananti, M., Petäjä, T., Piel, F., Pospisilova,
712 V., Quéléver, L. L. J., Rissanen, M. P., Rose, C., Sarnela, N., Schallhart, S., Schuchmann, S., Sengupta, K.,
713 Simon, M., Sipilä, M., Tauber, C., Tomé, A., Tröstl, J., Väisänen, O., Vogel, A. L., Volkamer, R., Wagner, A. C.,
714 Wang, M. Y., Weitz, L., Wimmer, D., Ye, P. L., Ylisirnio, A., Zha, Q. Z., Carslaw, K. S., Curtius, J., Donahue, N.
715 M., Flagan, R. C., Hansel, A., Riipinen, I., Virtanen, A., Winkler, P. M., Baltensperger, U., Kulmala, M., and
716 Worsnop, D. R.: Multicomponent new particle formation from sulfuric acid, ammonia, and biogenic vapors, Sci
717 Adv, 4, https://doi.org/10.1126/sciadv.aau5363, 2018.
718 Leino, K., Lampilahti, J., Poutanen, P., Väänänen, R., Manninen, A., Buenrostro Mazon, S., Dada, L., Franck, A.,
719 Wimmer, D., Aalto, P. P., Ahonen, L. R., Enroth, J., Kangasluoma, J., Keronen, P., Korhonen, F., Laakso, H.,
720 Matilainen, T., Siivola, E., Manninen, H. E., Lehtipalo, K., Kerminen, V.-M., Petäjä, T., and Kulmala, M.:
721 Vertical profiles of sub-3 nm particles over the boreal forest, Atmos Chem Phys, 19, 4127-4138,
722 10.5194/acp-19-4127-2019, 2019.
723 Liu, J., Zhang, X. L., Xu, X. F., and Xu, H. H.: Comparison analysis of variation characteristics of SO2, NOx,
724 O3 and PM2.5 between rural and urban areas, Beijing Huan jing ke xue= Huanjing kexue / [bian ji, Zhongguo
725 ke xue yuan huan jing ke xue wei yuan hui "Huan jing ke xue" bian ji wei yuan hui.], 29, 1059-1065, 2008.
726 Liu, J. Q., Jiang, J. K., Zhang, Q., Deng, J. G., and Hao, J. M.: A spectrometer for measuring particle size
727 distributions in the range of 3 nm to 10 mu m, Front Env Sci Eng, 10, 63-72,
728 https://doi.org/10.1007/s11783-014-0754-x, 2016.
729 Lee, B. P., Li, Y. J., Flagan, R. C., Lo, C., and Chan, C. K.: Sizing characterization of the fast mobility particle
730 sizer (FMPS) against SMPS and HR-ToF-AMS, Aerosol Sci. Technol., 47, 1030–1037,

https://doi.org/10.1080/02786826.2013.810809, 2013.

Lu, Y., Yan, C., Fu, Y., Chen, Y., Liu, Y., Yang, G., , Wang, Y., Bianchi, F., Chu, B., and Zhou, Y.: A proxy for atmospheric daytime gaseous sulfuric acid concentration in urban Beijing, Atmos Chem Phys, 19, 1971-1983, 10.5194/acp-19-1971-2019, 2019.

Ma, L., Zhu, Y., Zheng, M., Sun, Y., Huang, L., Liu, X., Gao, Y., Shen, Y., Gao, H., and Yao, X.: Investigating three patterns of new particles growing to the size of cloud condensation nuclei in Beijing's urban atmosphere, Atmos Chem Phys, 21, 183-200, 10.5194/acp-21-183-2021, 2021.

Man, H. Y., Zhu, Y. J., Ji, F., Yao, X. H., Lau, N. T., Li, Y. J., Lee, B. P., and Chan, C. K.: Comparison of Daytime and Nighttime New Particle Growth at the HKUST Supersite in Hong Kong, Environ Sci Technol, 49, 7170-7178, 2015.

Olauson, J.: ERA5: The new champion of wind power modelling?, Renewable Energy, 126, 322-331, 2018.

Paasonen, P., Peltola, M., Kontkanen, J., Junninen, H., Kerminen, V.-M., and Kulmala, M.: Comprehensive analysis of particle growth rates from nucleation mode to cloud condensation nuclei in boreal forest, Atmos Chem Phys, 18, 12085-12103, 10.5194/acp-18-12085-2018, 2018.

Pierce, J. R., and Adams P. J.: Uncertainty in global CCN concentrations from uncertain aerosol nucleation and primary emission rates. Atmos. Chem. Phys., 9, 1339–1356, 10.5194/acp-9-1339-2009, 2009.

Qi, X., Ding, A., Roldin, P., Xu, Z., Zhou, P., Sarnela, N., Nie, W., Huang, X., Rusanen, A., Ehn, M., Rissanen, M. P., Petäjä, T., Kulmala, M., and Boy, M.: Modelling studies of HOMs and their contributions to new particle formation and growth: comparison of boreal forest in Finland and a polluted environment in China, Atmos Chem Phys, 18, 11779-11791, 10.5194/acp-18-11779-2018, 2018.

Qi, X. M. D., A. J., Nie, W., Petaja, T., Kerminen, V. M., Herrmann, E., Xie, Y. N., Zheng, L. F., Manninen, H., Aalto, P., Sun, J. N., Xu, Z. N., Chi, X. G., Huang, X., Boy, M., Virkkula, A., Yang, X. Q., Fu, C. B., and Kulmala, M.: Aerosol size distribution and new particle formation in the western Yangtze River Delta of China: 2 years of measurements at the SORPES station, Atmos Chem Phys, 15, 12445-12464, 2015.

Salma, I., Borsós, T., Weidinger, T., Aalto, P., Hussein, T., Dal Maso, M., and Kulmala, M.: Production, growth and properties of ultrafine atmospheric aerosol particles in an urban environment. Atmospheric Chemistry and Physics. 11. 10.5194/acp-11-1339-2011,2011.

Salma, I., Németh, Z., Kerminen, V.-M., Aalto, P., Nieminen, T., Weidinger, T., Molnár, Á., Imre, K., and

759 Kulmala, M.: Regional effect on urban atmospheric nucleation, Atmos Chem Phys, 16, 8715-8728,
760 10.5194/acp-16-8715-2016, 2016.
761 Sellegri, K., Rose, C., Marinoni, A., Lupi, A., Wiedensohler, A., Andrade, M., Bonasoni, P., and Laj, P.: New
762 particle formation: A review of ground-based observations at mountain research stations, Atmosphere, 10, 493,
763 https://doi.org/10.3390/atmos10090493, 2019.
764 Shen, X., Sun, J., Kivekäs, N., Kristensson, A., Zhang, X., Zhang, Y., Zhang, L., Fan, R., Qi, X., Ma, Q., and
765 Zhou, H.: Spatial distribution and occurrence probability of regional new particle formation events in eastern
766 China, Atmos Chem Phys, 18, 587-599, 10.5194/acp-18-587-2018, 2018.
767 Shen, X. J., Sun, J. Y., Zhang, Y. M., Wehner, B., Nowak, A., Tuch, T., Zhang, X. C., Wang, T. T., Zhou, H. G.,
768 Zhang, X. L., Dong, F., Birmili, W., and Wiedensohler, A.: First long-term study of particle number size
769 distributions and new particle formation events of regional aerosol in the North China Plain, Atmos Chem Phys,
770 11, 1565-1580, 2011.
771 Stohl, A., Forster, C., Frank, A., Seibert, P., and Wotawa, G.: Technical note: The Lagrangian particle dispersion
772 model FLEXPART version 6.2. , Atmospheric Chemistry and Physics,5, 24, 10.5194/acp-5-2461-2005., 2005.
773 Vana, M., Komsaare, K., Hõrrak, U., Mirme, S., Nieminen, T., Petäjä, T., Noe, S. M., Kontkanen, J., Manninen,
774 H. E., , and Kulmala, M.: Characteristics of new-particle formation at three SMEAR stations, Boreal Environ
775 Res, 21, 17, 2016.
776 Wang, J., Shen, Y., Li, K., Gao, Y., Gao, H., and Yao, X.: Nucleation-mode particle pool and large increases in
777 Ncn and Nccn observed over the northwestern Pacific Ocean in the spring of 2014. , Atmos. Chem. Phys., 19,
778 17, https://doi.org/10.5194/acp-19-8845-2019, 2019.
779 Wang, M., Zhu, T., Zhang, J. P., Zhang, Q. H., Lin, W. W., Li, Y., and Wang, Z. F.: Using a mobile laboratory to
780 characterize the distribution and transport of sulfur dioxide in and around Beijing, Atmos Chem Phys, 11,
781 11631-11645, 2011.
782 Wang, Z. B., Hu, M., Sun, J. Y., Wu, Z. J., Yue, D. L., Shen, X. J., Zhang, Y. M., Pei, X. Y., Cheng, Y. F., and
783 Wiedensohler, A.: Characteristics of regional new particle formation in urban and regional background
784 environments in the North China Plain, Atmos Chem Phys, 13, 12495-12506, 10.5194/acp-13-12495-2013,
785 2013.
786 Wang, Z. B., Wu, Z. J., Yue, D. L., Shang, D. J., Guo, S., Sun, J. Y., Ding, A. J., Wang, L., Jiang, J. K., Guo, H.,

Gao, J., Cheung, H. C., Morawska, L., Keywood, M., and Hu, M.: New particle formation in China: Current knowledge and further directions, Science of the Total Environment, 577, 258-266, 2017.

Wu, Z., Hu, M., Liu, S., Wehner, B., Bauer, S., Ma ßling, A., Wiedensohler, A., Petäjä, T., Dal Maso, M., and Kulmala, M.: New particle formation in Beijing, China: Statistical analysis of a 1-year data set, Journal of Geophysical Research, 112, 10.1029/2006jd007406, 2007.

Yang-Chun, Y., Bo, H., and Wang, Y.: Changing Characteristics of the Main Air Pollutants of the Dongling Mountain in Beijing, Environmental Science, 34, 8, 2013.

Yao, L., Garmash, O., Bianchi, F., Zheng, J., Yan, C., Kontkanen, J., Junninen, H., Mazon, S. B., Ehn, M., Paasonen, P., Sipilä, M., Wang, M. Y., Wang, X. K., Xiao, S., Chen, H. F., Lu, Y. Q., Zhang, B. W., Wang, D. F., Fu, Q. Y., Geng, F. H., Li, L., Wang, H. L., Qiao, L. P., Yang, X., Chen, J. M., Kerminen, V. M., Petäjä, T., Worsnop, D. R., Kulmala, M., and Wang, L.: Atmospheric new particle formation from sulfuric acid and amines in a Chinese megacity, Science, 361, 278-281, https://doi.org/10.1126/science.aao4839, 2018.

Yao, L., Fan, X., Yan, C., Kurtén, T., Daellenbach, K. R., Li, C., Wang, Y., Guo, Y., Dada, L., and Rissanen, M. P., Cai, J., Tham, Y. J., Zha, Q., Zhang, S., Du, W., Yu, M., Zheng, F., Zhou, Y., Kontkanen, J., Chan, T., Shen, J., Kujansuu, J. T., Kangasluoma, J., Jiang, J., Wang, L., Worsnop, D. R., Petäjä, T., Kerminen, V.-M., Liu, Y., Chu, B., He, H., Kulmala, M., and Bianchi, F.: Unprecedented Ambient Sulfur Trioxide (SO3) Detection: Possible Formation Mechanism and Atmospheric Implications, Environ Sci Tech Let 7, 809-818, 10.1021/acs.estlett.0c00615, 2020.

Ying, G., Ma, J., and Xing, Y.: Comparison of air quality management strategies of PM10, SO2, and NOx by an industrial source complex model in Beijing, Environmental Progress, 26, 33-42, 2010.

Yu, F. and Luo, G.: Simulation of particle size distribution with a global aerosol model: contribution of nucleation to aerosol and CCN number concentrations, Atmos. Chem. Phys., 9, 7691–7710, 10.5194/acp-9-7691-2009, 2009.

Zhang, J., Chen, Z., Lu, Y., Gui, H., Liu, J., Wang, J., Yu, T., and Cheng, Y.: Observations of New Particle Formation, Subsequent Growth and Shrinkage during Summertime in Beijing, Aerosol Air Qual Res, 16, 1591-1602, 10.4209/aaqr.2015.07.0480, 2016.

Zhou, Y., Dada, L., Liu, Y., and Fu, Y., Kangasluoma, J., Chan, T., Yan, C., Chu, B., Daellenbach, K. R., Bianchi, F., Kokkonen, T. V., Liu, Y., Kujansuu, J., Kerminen, V.-M., Petäjä, T., Wang, L., Jiang, J., and Kulmala, M.:

Variation of size-segregated particle number concentrations in wintertime Beijing, Atmos Chem Phys, 20, 1201-1216 10.5194/acp-20-1201-2020, 2020.

Zimmerman, N., Jeong, C.-H., Wang, J. M., Ramos, M., Wallace, J. S., and Evans, G. J.: A source-independent empirical correction procedure for the fast mobility and engine exhaust particle sizers, Atmos. Environ., 100, 7, 838 10.1016/j.atmosenv.2014.10.054, 2015., 2015.

Tables and Figures

Table 1: NPF event and non- event days during our observation at both stations.

Date	Type	Air masses (9:00-15:00)		$GR_{7\text{-}15nm}$ (nm/h)		J_7 ($cm^{-3}s^{-1}$)		Event Start (LT)		Ending diameter (nm)		CS (s^{-1})	
		UB	MT	UB	MT	UB	MT	UB	MT	UB	MT	UB	MT
2019/06/14	a	North	North	8.61	-	4.97	-	9:00	8:00	71	-	0.017	0.008
2019/06/15*	a	Local	Local	12.63	-	5.56	-	11:00	15:00	82	60	0.013	0.029
2019/06/17	d	East	Local									0.031	0.011
2019/06/18	c	Local	West		10.5		0.17		12:00		45	0.039	0.008
2019/06/19	d	South	Local									0.037	0.047
2019/06/21	d	East	Local									0.035	0.018
2019/06/23	e	East	East									0.033	0.013
2019/06/24	f	Local	Local		8.21		-		12:00		50	0.027	0.014
2019/06/25*	a	Local	Local	-	-	-	-	12:00	15:00	-	53	0.032	0.027
2019/06/28	g	West	West	-		-		11:00				0.022	0.006
2019/06/29	a	North	North	12.93	7.14	6.93	2.28	9:00	8:00	21	19	0.008	0.011
2019/06/30	a	North	North	4.82	6.57	9.86	1.37	6:30	9:30	31	25	0.003	0.008
2019/07/01	a	North	North	7.31	5.82	3.84	0.82	9:00	8:30	105	102	0.006	0.009
2019/07/02	d	Local	West									0.013	0.014
2019/07/03	a	North	North	7.89	6.52	3.25	0.75	9:00	8:00	72	46	0.015	0.006
2019/07/04	b	Local	Local	-		-		10:00		53		0.012	0.012
2019/07/06	a	North	North	7.39	6.51	9.21	1.75	7:00	9:30	25	19	0.004	0.011
2019/07/07	b	North	North	7.61		3.61		9:00		32		0.008	0.005
2019/07/08	d	East	East									0.019	0.012
2019/07/09	d	East	East									0.021	0.015
2019/07/10	h	East	East									0.017	0.013
2019/07/11	d	East	East									0.039	0.014

2019/07/12	f	East	East		5.57		0.37		9:30		24	0.018	0.014
2019/07/13	c	Local	North		6.32		0.70		10:00		30	0.037	0.012
2019/07/14	a	North	North	12.04	9.86	3.91	0.89	9:30	9:30	63	47	0.023	0.017

825 'a' means NPF event observed at both stations, 'b' means NPF event day at UB station while non-event day at
826 MT station, 'c' means NPF event day at MT station while non-event day at UB station, 'd' means non-event day
827 at both stations on the same day, 'e' means undefined day at both stations, 'f' means undefined day at UB station
828 while NPF event day at MT station, g means undefined day at MT station while NPF event day at UB station, h
829 means undefined day at UB station while non-event day at MT station, * means NPF event observed at MT
830 station was transported from somewhere else. – means the values cannot be reliably calculated. Only days when
831 particle number size distribution were valid are included in this table.
832

Figure 1: Map showing locations of urban station (UB), Longquan station (LQ), and mountain station (MT). Image is produced using © Google Maps.

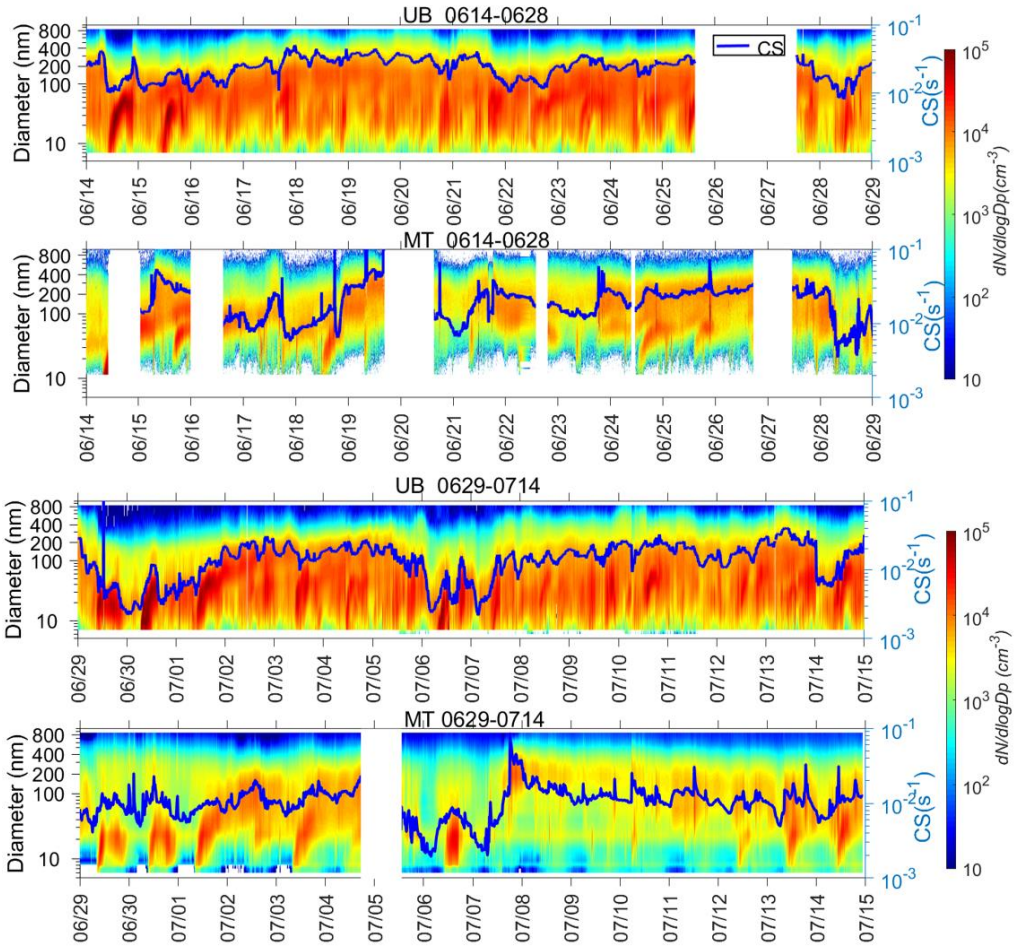

838

839 **Figure 2: Time series of particle number size distribution and CS (the blue line) at UB and MT stations during our**

840 **observations. Time resolutions for particle number size distribution data and CS were 8 min at UB station and 4 min**

841 **at MT station, respectively.**

842

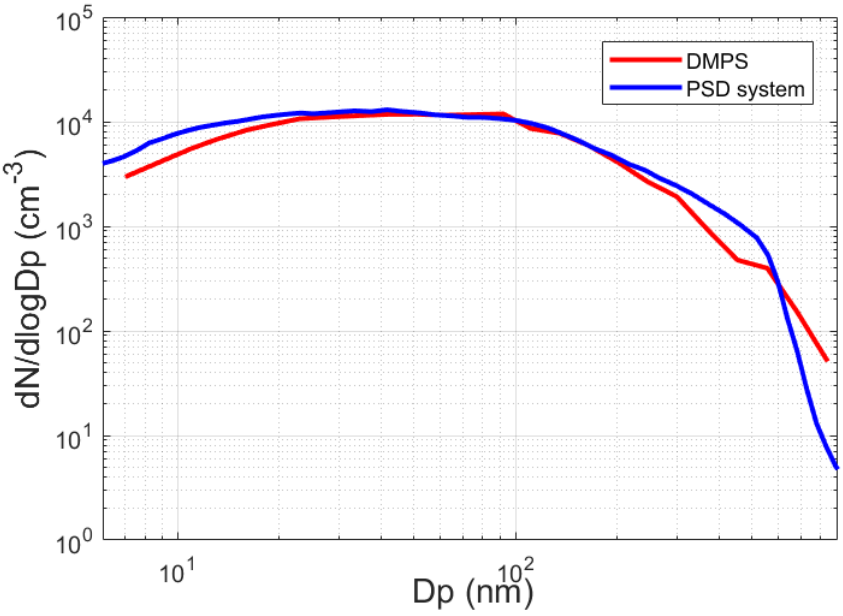

843

844 **Figure 3: Median particle number size distribution in 5-900 nm measured by DMPS and PSD during our observation**

845 **from June 1 to August 31, 2019 at UB station. The time window of the data is from 9:00-15:00 of every day.**

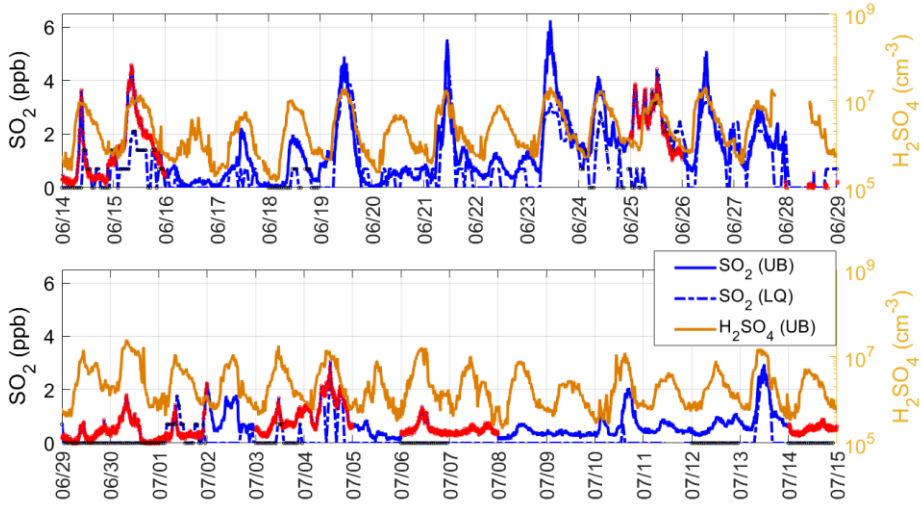

846

847 **Figure 4: Time series of SO_2 concentration (ppb) at UB station and Longquan station (LQ) during our observation**

848 **(left axis) as well as H_2SO_4 concentration measured at UB station (right axis). Data under detection limit are set as**

849 **zero at both stations. Data on NPF event days were marked in red at UB station and black at MT station. Time**

850 **resolution for SO_2 data was 5 min at UB station and 1h at LQ station, respectively.**

851

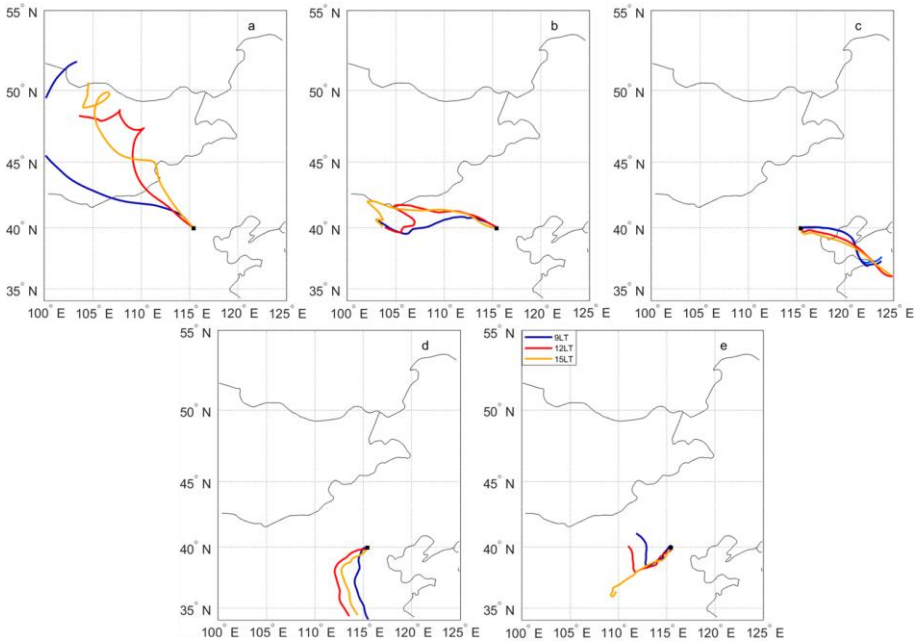

852

853 **Figure 5: Examples of air masses arrived at both stations from (a) North group, (b) West group, (c) East group, (d)**

854 **South group and (d) Local group during 9:00-15:00 (local time, LT). Both stations are under the same marker.**

855

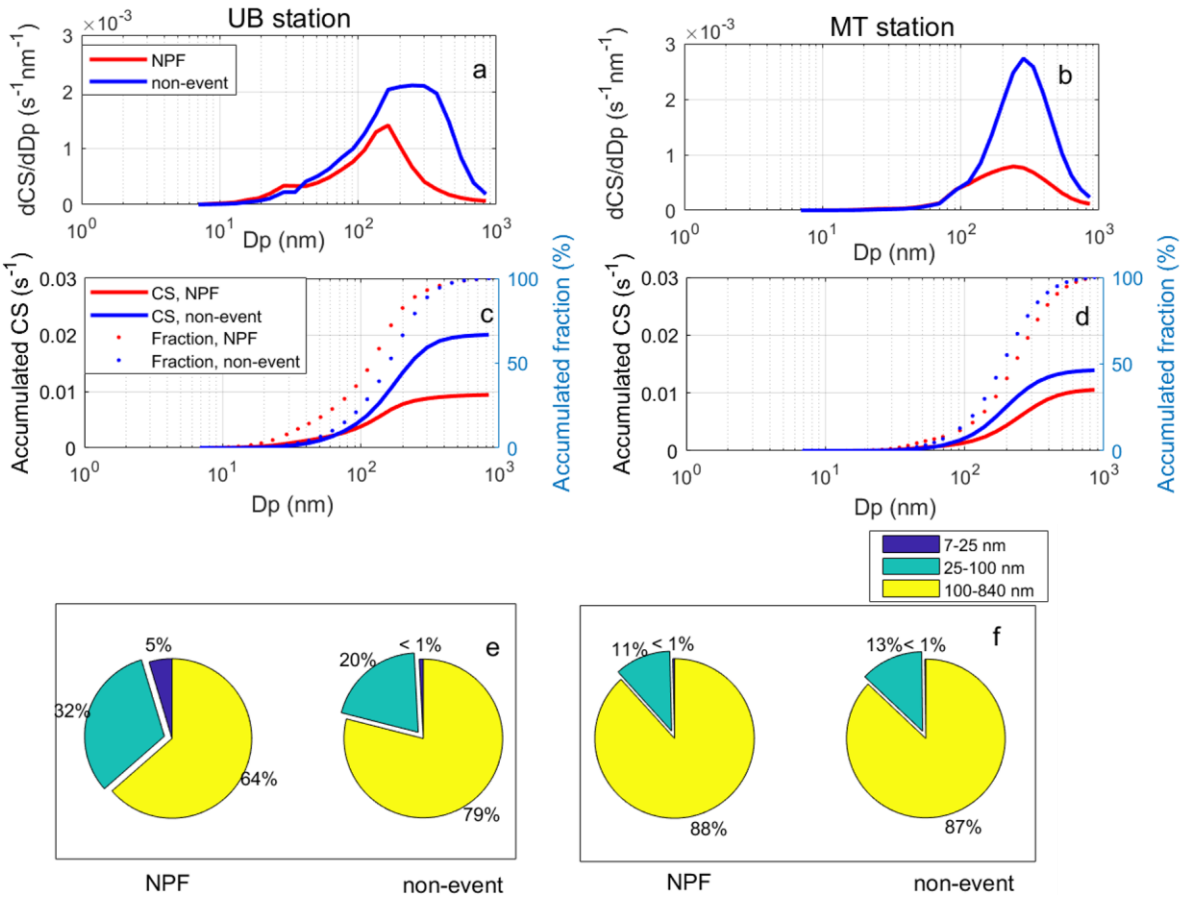

Figure 6: Median CS size distribution (a&b), accumulated CS contributed by particles from 6 nm and the ratio between accumulated CS and total CS (c&d); Contribution of size-segregated particles to total CS (e&f) at each site on NPF and non-event days during 9:00-15:00 (local time, LT). Figures on the left and right panels represented data observed at UB and MT site, respectively. The time resolutions for CS and particle number concentration data were 8 min at UB station and 4 min at MT station, respectively.

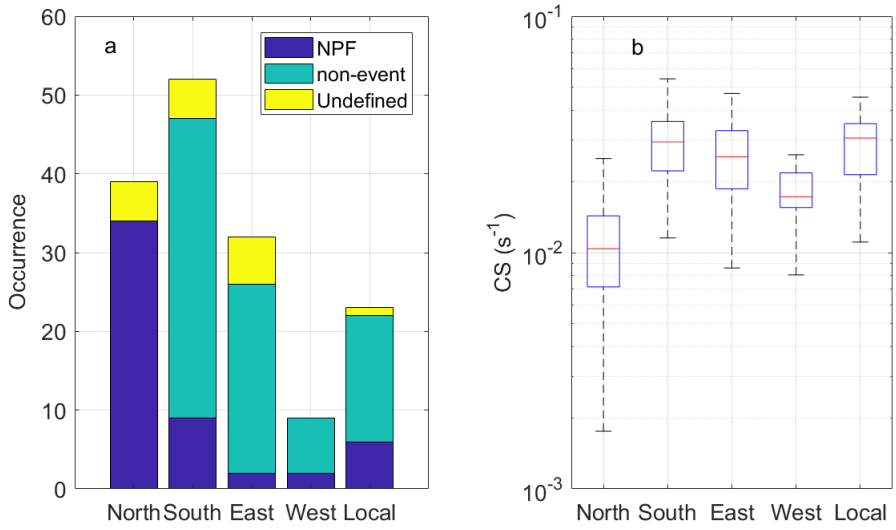

Figure 7: Occurrence of NPF events and non-events under air masses arriving from different directions (a) as well as medians and percentiles of condensation sink (CS, s^{-1}) during the 9:00-11:00 (local time) under different air masses (b) during our observation in summer 2018 and 2019 at UB station. The red line represents the median of the data and the lower and upper edges of the box represent 25th and 75th percentiles of the data, respectively. The length of the whiskers represents 1.5× interquartile range which includes 99.3% of the data. Data outside the whiskers are considered outliers and are marked with red crosses. The time resolution of CS was 8 min.

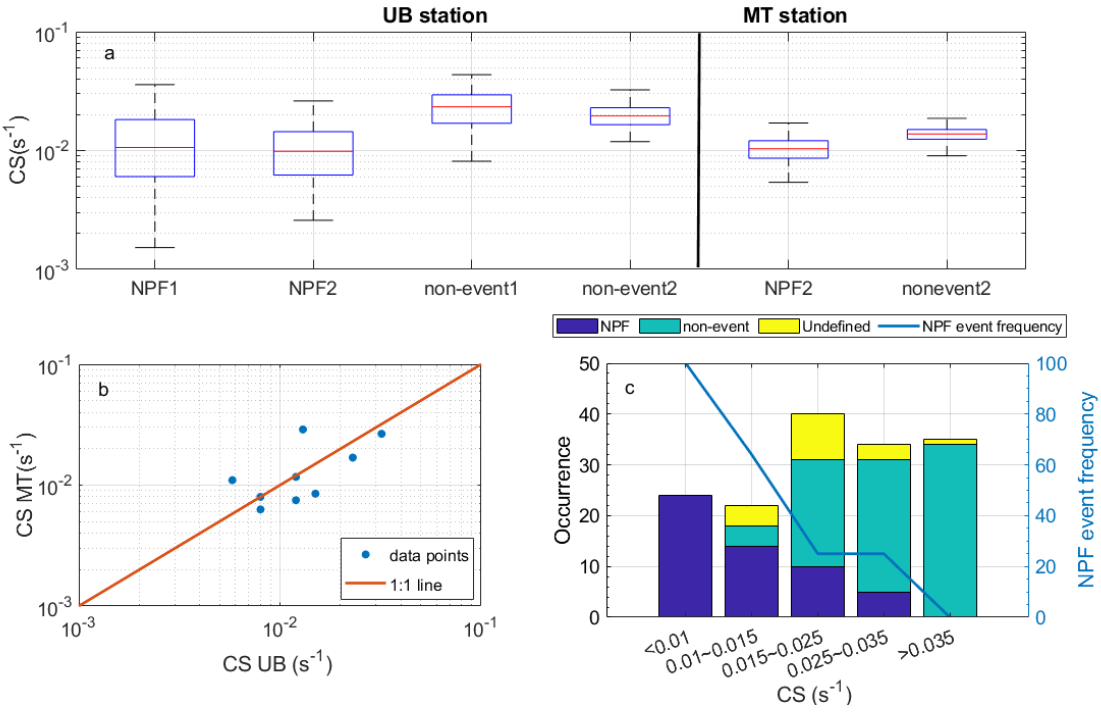

872

873 **Figure 8: (a) Median and percentiles of condensation sink (CS, s^{-1}) during our observations at both stations. The**
874 **'NPF1' and 'non-event1' referred to NPF and non-event days during summer 2018 and 2019, while 'NPF2' and**
875 **'non-event2' referred to NPF and non-event days during the short-term parallel observation from June 14 to July 14,**
876 **2019 at both sites. The red line represents the median of the data and the lower and upper edges of the box represent**
877 **25th and 75th percentiles of the data, respectively. The length of the whiskers represents 1.5× interquartile range which**
878 **includes 99.3% of the data. The time resolution of CS was 8 min. (b) Median CS during the first 2 hours of NPF**
879 **events on common NPF event days measured at both stations (MT vs. UB) . (c) Numbers of NPF event, non-event and**
880 **undefined days as well as NPF event frequency as a function of CS during our observation in summer 2018 and 2019**
881 **at UB station.**

882

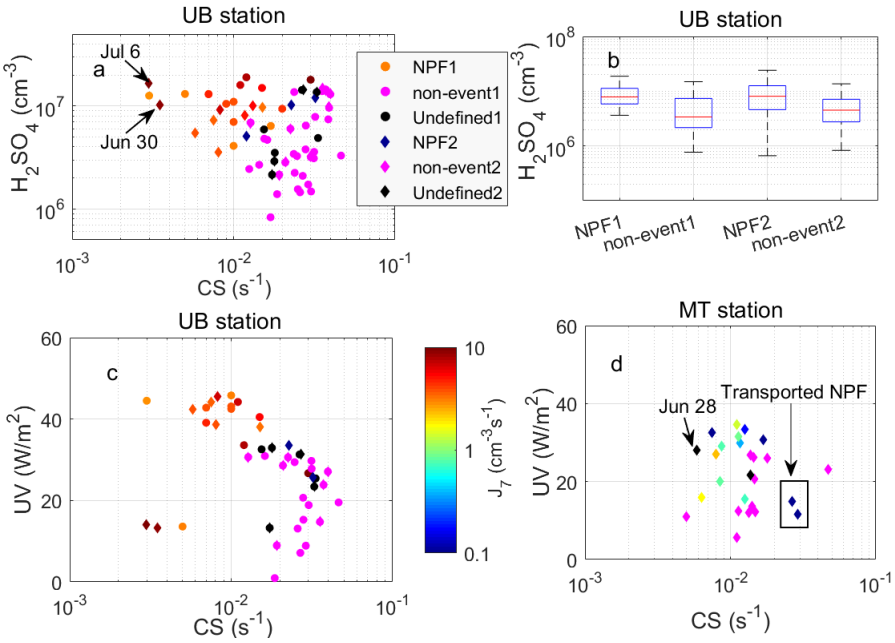

883

884 **Figure 9: (a) Median condensation sinks (CS, s^{-1}) and H_2SO_4 concentration (SA, cm^{-3}) and (b) (b) medians and**
885 **percentiles of H_2SO_4 concentration observed at UB station during the first 2 hours of NPF events and 9:00-11:00 on**
886 **non-event days. (c) solar radiation (UVA+UVB, W/m^2) during the first 2 hours of every NPF event and 9:00-11:00 on**
887 **every non-event day at UB station. The 'NPF1' and 'non-event1' referred to NPF event and non-event days in**
888 **summer 2018 and 2019 and the 'NPF2' and 'non-event2' referred to NPF event and non-event days during the**
889 **observation from June 14 to July 14, 2019. (d) Median condensation sinks (CS, s^{-1}) and solar radiation (UVA+UVB,**
890 **W/m^2) during the first 2 hours of every NPF event and 9:00-11:00 on every non-event day at MT station. Transported**
891 **NPF event cases and one non-event day with air masses belonging to west group (Jun 28) were all pointed out in the**
892 **figure. Size of data points on NPF event days means formation rate (J_7, $cm^{-3}s^{-1}$) when it can be calculated reliably. The**
893 **time resolution of CS was 8 min at UB station and 4 min at MT station, respectively. The time resolution was 30 min**
894 **for SA data at UB station and 1h for solar radiation data at both stations.**

895

896

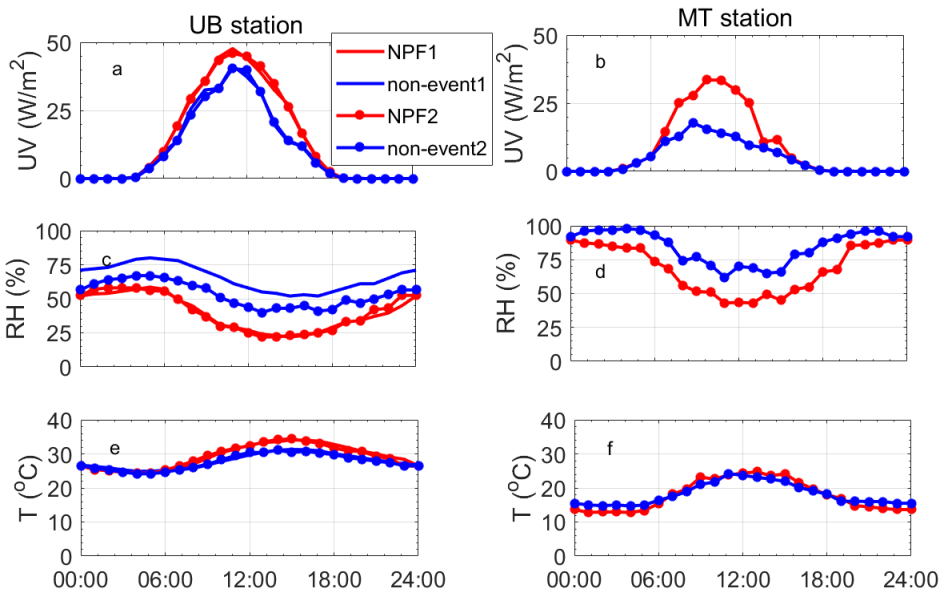

Figure 10: (a, b) Diurnal pattern of solar radiation (UV, W/m^2), (c, d) Temperature (T, °C), and (e, f) Relative humidity (RH, %), at UB (left panel) and MT (right panel) stations on both NPF event and non-event days. Time resolutions for all data points here were 1h. The 'NPF1' and 'non-event1' referred to NPF event and non-event days in summer 2018 and 2019 and the 'NPF2' and 'non-event2' referred to NPF event and non-event days during the observation from June 14 to July 14, 2019.

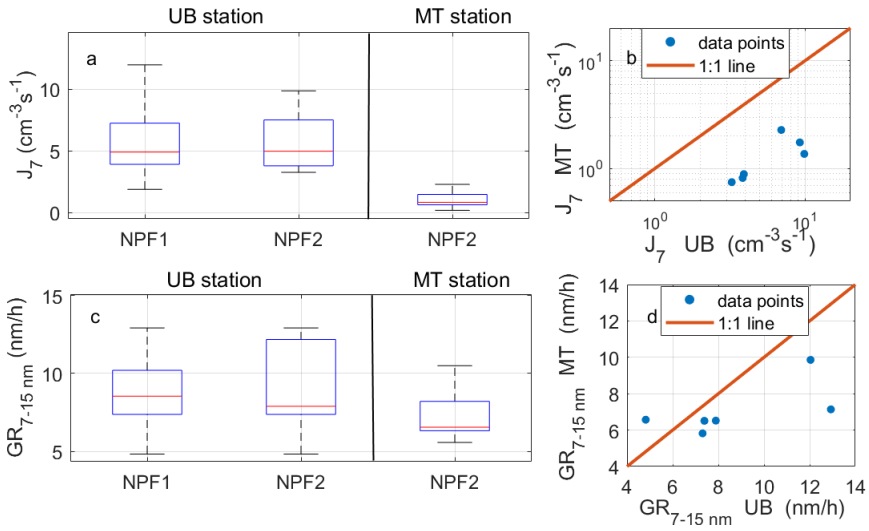

904

905 **Figure 11: Median and percentages of formation rates of 7 nm (J_7, cm^{-3}s^{-1}) (a) and growth rates from 7 to 15 nm**
906 **($GR_{6\text{-}15\ nm}$, nm/h) (c) measured at both stations during our observation as well as comparison between J_7 (b) and**
907 **$GR_{6\text{-}15\ nm}$ (d) of common NPF events. The red line represents the median of the data and the lower and upper edges of**
908 **the box represent 25th and 75th percentiles of the data, respectively. The length of the whiskers represents 1.5×**
909 **interquartile range which includes 99.3% of the data. The 'NPF1' and 'non-event1' referred to NPF event and**
910 **non-event days in summer 2018 and 2019 and the 'NPF2' and 'non-event2' referred to NPF event and non-event days**
911 **during the observation from June 14 to July 14, 2019.**

912

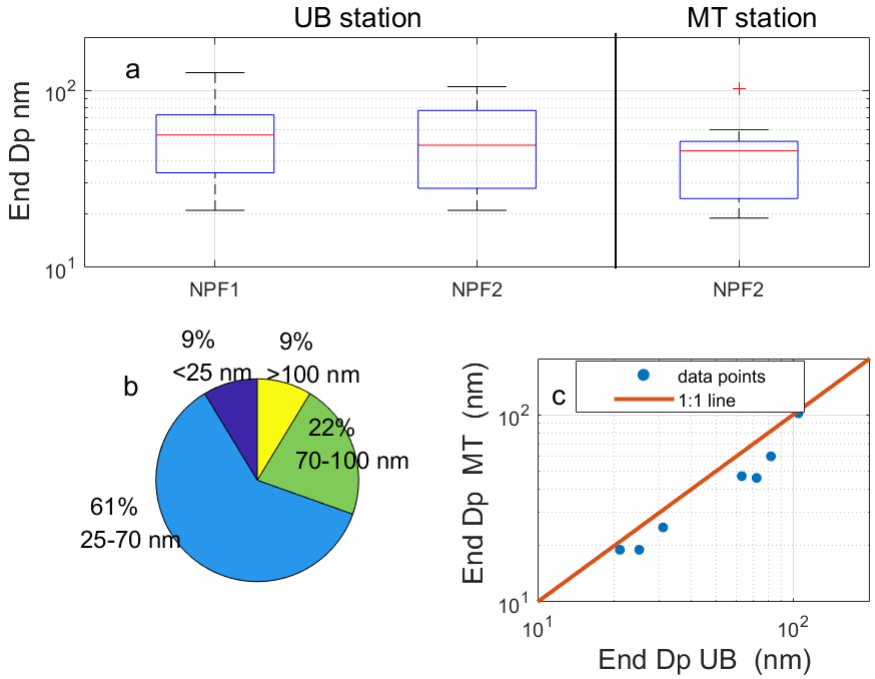

913

914 **Figure 12: (a) Median and percentiles of end diameters (End Dp, nm) of NPF events measured at both sites. The red**
915 **line represents the median of the data and the lower and upper edges of the box represent 25th and 75th percentiles of**
916 **the data, respectively. The length of the whiskers represents 1.5× interquartile range which includes 99.3% of the**
917 **data. The 'NPF1' and 'non-event1' referred to NPF event and non-event days in summer 2018 and 2019 and the**
918 **'NPF2' and 'non-event2' referred to NPF event and non-event days during the observation from June 14 to July 14,**
919 **2019. (b) Frequencies of end diameters in the size range of smaller than 25 nm, 25-70 nm, 70-100 nm and above 100**
920 **nm during our observation at UB station in summer 2018 and 2019. (c) Comparison between end diameters of**
921 **common NPF events at both stations.**

922

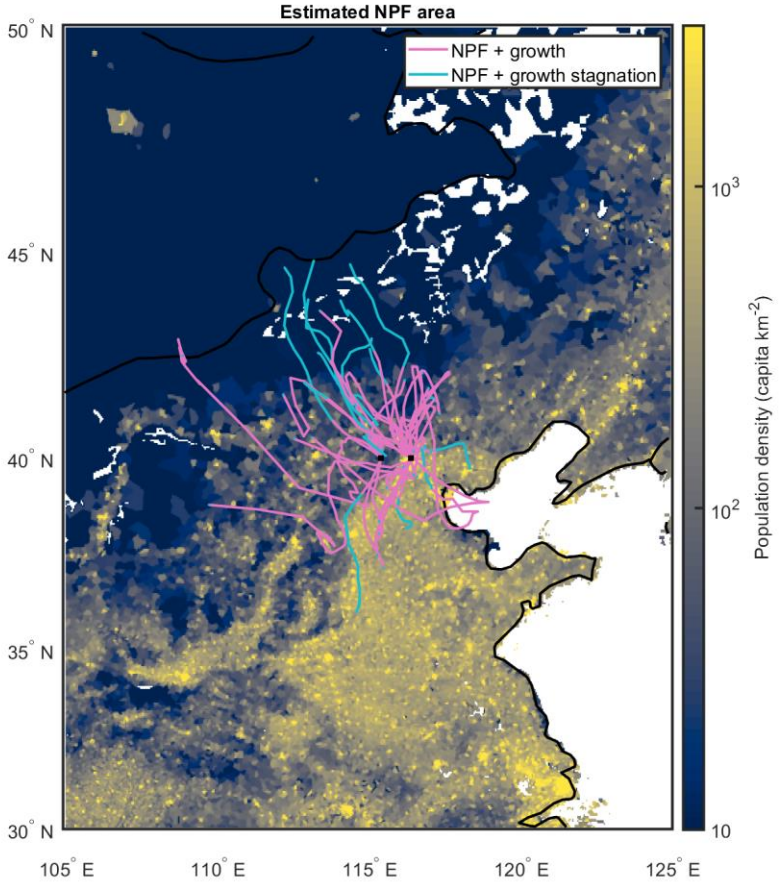

923

924

925 **Figure 13: Spatial extent of the area where new particle formation events are estimated to have taken place based on**
926 **air mass back trajectories and the observed NPF events at both sites. Each line represents a single NPF event and**
927 **extends to the point beyond which continuation of the mode formed in an NPF event was no longer observed at the**
928 **measurement site. In other words, if an air mass is located outside the area roughly outlined by the colored lines**
929 **during the typical onset time of NPF and then transported to our measurement sites, NPF is unlikely to have occurred**
930 **in said air mass. The lines change color from pink to light blue if the observed NPF event enters a stage of growth**
931 **stagnation, which can indicate a less favorable environment for the formation and growth of new particles. The lines**
932 **are overlaid on top of a population density map (Gridded Population of the World; GPWv4.10; CC BY 4.0), which is**
933 **used to illustrate the level of anthropogenic activities and emissions.**

934

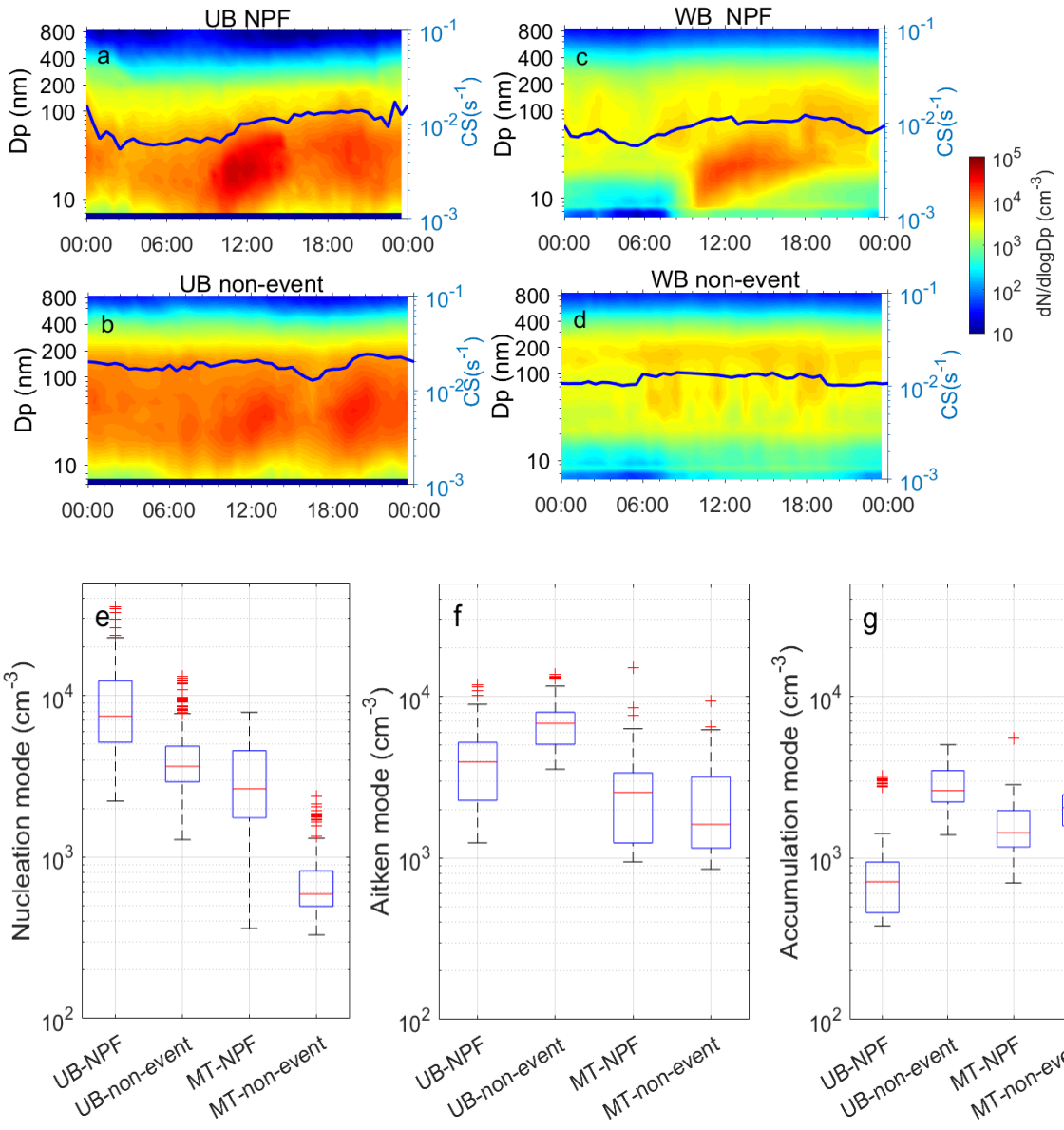

Figure 14: Median particle number size distribution as well as CS (blue lines) on NPF event and non-event days at UB (a&b) and MT (c&d) stations and median and percentiles of nucleation (e), Aitken (f) and accumulation (g) modes particle number concentration on NPF event and non-event days during our observation from June 14 to July 14, 2019 at both stations. The red line represents the median of the data and the lower and upper edges of the box represent 25th and 75th percentiles of the data, respectively. The length of the whiskers represents 1.5× interquartile range which includes 99.3% of the data. Data outside the whiskers are considered outliers and are marked with red crosses.

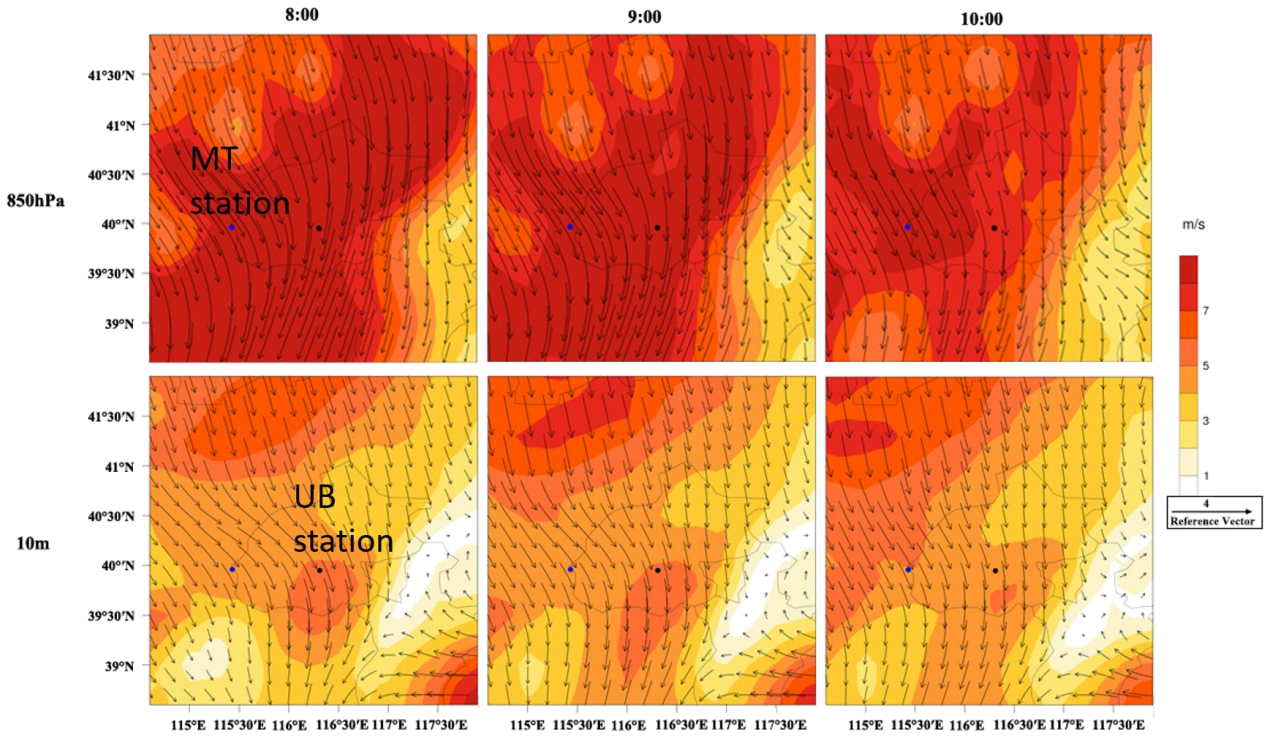

Figure 15: Wind distribution at 8:00, 9:00 and 10:00 on June 30, 2019 at 10 m above the ground level (lower panel) and 850 hPa (close to the altitude of MT station, upper panel). The blue and black points on the figures represent MT and UB stations, respectively.